INFORMATION TO USERS

This manuscript has been reproduced from the microfilm master. UMI films the text directly from the original or copy submitted. Thus, some thesis and dissertation copies are in typewriter face, while others may be from any type of computer printer.

The quality of this reproduction is dependent upon the quality of the copy submitted. Broken or indistinct print, colored or poor quality illustrations and photographs, print bleedthrough, substandard margins, and improper alignment can adversely affect reproduction.

In the unlikely event that the author did not send UMI a complete manuscript and there are missing pages, these will be noted. Also, if unauthorized copyright material had to be removed, a note will indicate the deletion.

Oversize materials (e.g., maps, drawings, charts) are reproduced by sectioning the original, beginning at the upper left-hand corner and continuing from left to right in equal sections with small overlaps.

Photographs included in the original manuscript have been reproduced xerographically in this copy. Higher quality 6" x 9" black and white photographic prints are available for any photographs or illustrations appearing in this copy for an additional charge. Contact UMI directly to order.

Bell & Howell Information and Learning
300 North Zeeb Road, Ann Arbor, MI 48106-1346 USA
800-521-0600

Université d'Ottawa · University of Ottawa

Study of Surface Flattening Kinetics by Low Energy Electron Diffraction on Rutile (110)

By

Aiguo Cai

Thesis
Submitted to the School of Graduate Studies and Research of
the University of Ottawa
in the fulfillment of the thesis requirements
for the degree of

Master of Science
in Physics

University of Ottawa
Ottawa, Ontario
August 16th, 2000

Abstract

In this thesis, we study the surface flattening kinetics at a roughened rutile (1×1)(110) surface in an ultrahigh vacuum chamber by low energy electron diffraction spot profile analysis(SPA-LEED). Surface roughness was introduced by argon ion bombardment at a low sputtering dose, instead of deposition such as molecular beam epitaxy(MBE) used elsewhere. The time-resolved results of the flattening kinetics show that the average terrace width increases with annealing time to follow power-law behavior $l(t) \propto t^{\beta}$ with scans in the [-110] and [001] directions, giving the flattening exponent $\beta=0.24\pm0.04$ in the range of annealing temperature 800-850K. The flattening exponent β after the low sputtering dose is similar to that of previous work done by Piercy and Grossmann[1,2] after a higher sputtering dose; they found $\beta= 0.23$-0.25 in the range of temperature 800-850K.

In addition, we further investigated the effect of annealing on the terrace height distribution by measuring spot profiles versus incident electron energy at room temperature after annealing for different times. The terrace height distribution was determined by analyzing the relative weight of the Bragg peak in the spot profiles versus the incident electron energy. The analyzed results show that the low sputtering dose produces a terrace height distribution different from that of the higher sputtering dose. With increasing annealing time the coverage at each level stays nearly constant after the low or higher sputtering dose. By means of the results of the terrace height distribution the interface width versus annealing time was determined. For the low dose case, the interface width slightly reduces with increasing annealing time and equals about 2.2Å, while, for the higher dose, the interface width slightly increases with increasing annealing time and stays at about 3.0Å. From the above experimental results and analysis, we can further deduce that, for this few-level system, diffusion of atoms at the surface takes place only at the same level while the probability of atoms

jumping from one layer to others is quite small. This might come from the effect of surface step potential barriers but the detailed effect of the potential barriers at steps on diffusing atoms is not clear. This needs to be researched further.

Acknowledgments

I would like to express my sincere gratitude to Dr. Peter Piercy, my research supervisor, for his great support, patient guidance and continued encouragement. He is one of the best professors I meet in my life. His knowledge is very profound in the field of surface science. If I had not got his great help, I would not finish the study of Master Degree as well as the thesis. Working with him has been extremely rewarding.

I would also like to thank Dr. Bruno J. Riel, my good friend, for his great help. For his encouragement and support, I not only obtained confidence to overcome difficulties but also learnt many new applications of physics such as quantum wells and dots by MBE from him.

As well, I would like to thank Mr. Stone X. D. Zhang, the first director of Contonia International Inc., and my good friend, very much for his support and help so that I kept my mind on study and I thank him to provide much more new information so that I know the application of surface physics in integrated circuits.

Finally, I also thank Xiaohe Cheng, my wife, for her great support and help. She accepts all the house work and looks after our daughter and, at the same time, I thank Yin Cai, my daughter, for her support.

Table of Contents

List of Figures

List of Tables

Chapter 1. Introduction

1.1 Experimental Motivation

In recent decades surface science has been paid more attention by all the areas of science because of its extensive applications such as semiconductor devices, optical components, heterogeneous catalysis, metallurgical materials and so on [3,4]. It can be said without any exaggeration that the technological foundation of most high-tech industries is based primarily on research and development of surface science [5]. What is surface science? Surface science is the study of surface structures and properties of materials at the atomic scale. It involves many disciplines in science such as surface physics, physical chemistry, ultrahigh vacuum technique, electron diffraction technique, and material science. Why do we research surfaces? Because different materials have different surface structures, the different surface structures result in different physical and chemical properties. Therefore, we can use the different properties to make different components such as semiconductor lasers, optical filters, and large-scale integrated circuits and so on.

A particularly interesting problem in the field of surface research is to understand diffusion-flattening mechanisms of surface growth fronts. Although the subject has been researched for decades, many important physical mechanisms on surfaces are still not very clear. In this thesis, we mainly focus on investigation of surface flattening kinetics by experimental methods. When a roughened surface is annealed below its roughening transition temperature, the surface will become flatter and flatter with increasing annealing time. This process is referred to as flattening kinetics. During annealing, atoms at the surface diffuse from regions of higher chemical potential to those of lower potential so that the free energy of the surface tends to reach a minimum. This is the mechanism of flattening at a surface. In an actual situation, the mechanism may be complicated since it not only

involves atomic diffusion at the surface but may also include atomic diffusion in the volume of the solid as well as mass transport by evaporation and condensation. Those factors depend on the structure of the surface. Our investigation of surface flattening kinetics was based on previous work by Piercy and Grossmann[1,2] but we used a low sputtering dose to remove less than one monolayer and to produce a surface spanning a few levels, while the previous work done by Piercy and Grossmann used a higher sputtering dose to remove more than ten monolayers. In the two different initial conditions, we checked whether the flattening exponent values were the same or not. In the low dose case, we compared the experimental results of the flattening exponent with the theory of surface flattening kinetics. Besides the measurements of the flattening exponent, we also investigated the effect of annealing on the terrace height distribution. By determining the terrace height distribution after different annealing times, we could hope to understand better the mechanism of atomic diffusion at the surface of a crystal surface when the interface width is small.

1.2 History of Study on Surface Flattening Kinetics

From theoretical papers, we found that as early as 1958, Mullins [6], based on his previous work [7] and others [8, 9,10], put forward the classical continuum theory of flattening of a nearly plane solid surface. Supposing the surface is initially corrugated, having a one-dimensional sinusoidal variation in height versus lateral position, he showed that surface flattening followed $\tau \propto \lambda^4$ when limited by surface diffusion, where λ is the wavelength of the corrugation and τ is the lifetime. His theoretical model can only be applied above the roughening transition temperature, T_R, since, in this range, a surface has a rounded microscopic morphology so that his assumptions can be met. However, below T_R, the surface exhibits facets which are microscopically flat so that there must be a cusp in the surface tension $\gamma(\theta)$ at $\theta=0$. As a result, Mullins' theory fails below T_R . For a bidirectional groove geometry at a crystal surface with steps, Rettori and Villain [11] used a discrete chemical potential $\mu_n(l)$ for an atom on an edge of the n^{th} terrace with average radius R_n to derive that

the characteristic time τ for amplitude decay of a sinusoidally grooved surface is proportional to $h(0)\lambda^3$ below T_R, where λ indicates the wavelength and h(0) is the initial amplitude. From this relationship, we can see that if h(0) is constant, then $\tau \propto \lambda^3$. This result is similar to that of the model of two-dimensional island growth in which the average island radius R grows as $R \propto t^{1/3}$ [12]. If h(0) is initially proportional to λ, then $\tau \propto \lambda^4$ which is similar to that of the model of three-dimensional island growth[13]. Uwaha[14] studied the relaxation of the crystal shape caused by step motion and found that the facet size at a crystal surface expands as $R_f \propto t^{1/5}$. In order to study the surface flattening exponent, many researchers [15,16,17,18,19,20] used a solid-on-solid model and the Monte Carlo method to carry out simulations of flattening kinetics for a sinusoidally corrugated crystal surface using a computer. Among them, Searson and Li[15] found the characteristic time scale $\tau \propto \lambda^4$ for decay of a unidirectional or bidirectional sinusoidal surface modulation below and above T_R. Jiang and Ebner [18] also discovered that the surface relaxation initially follows an exponential decay with a characteristic time that scales as the fourth power of the grooves' wavelength below T_R, and then the scaling behavior breaks down after plateaus of a sufficient size develop at the top and bottom of the profile. The results of Erlebacher and Aziz[20] show that τ for a bidirectional sinusoidal surface modulation with wavelength λ was found to scale as λ^3, while for a unidirectional sinusoidal surface modulation, τ approximately followed λ^4.

The above theories of surface flattening kinetics were mainly tested by measurements of the height decay of corrugated surfaces, using light interference micrographs. However, for a microscopically rough surface, this experimental method does not work. So, other experimental methods have to be used. So far, there are two other methods to research crystal surface morphology. One is diffraction techniques such as low energy electron diffraction (LEED), medium energy electron diffraction (MEED), reflection high energy electron diffraction (RHEED), X-ray, and atom-beam diffraction [5,21,22]; the other is imaging techniques such as the scanning tunnel microscope (STM) and transmission electron microscope (TEM) [23, 24]. Diffraction methods can provide more

accurate and quantitative data on average distances, distributions and probabilities, while imaging methods show the surface morphology directly, through which qualitative evaluation of surface defects such as steps and point defects is obtained. An imaging method can provide confirmation of the results by a diffraction method. Among these methods of surface research, high resolution low energy electron diffraction (HRLEED) is most suitable for investigating surface flattening kinetics because low energy electrons with energy in the range10eV-1000eV not only possess a minimum mean free path of about a few atomic spacings in solids[25], but also low energy electron diffraction can be used to determine the average terrace width easily.

The LEED method was developed and used in the late 1960s [26, 27]. Henzler et.al [28, 29, 30] were among the first to apply LEED spot profile analysis to carry out research and analysis of surface structures and defects. They developed the method, in which an angular spot profile from low energy electron diffraction may be divided into both a Bragg peak and a diffuse shoulder (due to the terrace height distribution). After that, Lent and Cohen [31] theoretically studied the diffraction intensity from a reversible stepped surface and derived the diffraction intensity as a function of coverage θ. Based on Lent and Cohen's work, Pukite et. al[32] further studied the diffraction intensity from stepped surfaces with arbitrary terrace distributions as a function of coverage θ. Although their formulas are general, they have not been applied practically due to their complication. Altsinger and Henzler [33] gave a simpler method of analyzing the surface terrace height distribution by measuring spot profiles and determining the relative weight $G_0(k_\perp)$ of the Bragg peak. Wollschager [34] used a similar method to investigate the effect of annealing on defects at the Si(111)/SiO_2 interface and found that annealing does not drastically improve the interface width but it reduces inhomogeneities drastically. Zuo and Wendelken[35] studied the smoothing kinetics of a rough surface after depositing ~100 monolayers of Cu on Cu (100) near room temperature by using time-resolved SPA-LEED. Their results show that, in early annealing times, the average terrace width l(t) increases as $t^{1/3}$ and follows $t^{1/5}$ in later times. Yang, Wang, and Lu[36] used MBE to deposit 250-450 Å of Si on Si(111)

and then measured the flattening kinetics of an initially rough Si(111) surface. Their results show that at low annealing temperature (<400°C).the average terrace width l(t) increases as $1/(\ln(1+\tau/t))^{1/4}$ and at temperature higher than 500°C, the slower dynamics only occurs at the initial stage, which is followed by a faster evolution with $l(t) \propto t^{1/5}$. Chey, Nostrand and Cahill[37] researched the dynamics of a rough Ge(001) surface at low temperatures (245-325°C) by using STM. Their result indicates that the lateral correlation length L increases as $t^{1/n}$ where n= 2.2±0.4. Piercy and Grossmann[1,2] used argon ion sputtering to produce a roughened TiO_2 (110) surface at a higher dose and then studied the flattening kinetics of the roughened surface. Their experimental results show that the flattening exponent β ($l(t) \propto t^{\beta}$) is 0.23-0.25 in the range of temperature 800-850K.

1.3 Sample: Rutile (TiO_2) Structure

TiO_2 is a metal oxide and occurs in three different crystal structures which are termed anatase, brookite, and rutile, respectively. It is a very abundant material and occurs naturally with relatively pure form as the mineral rutile whose crystalline structure is shown in figure 1.1.

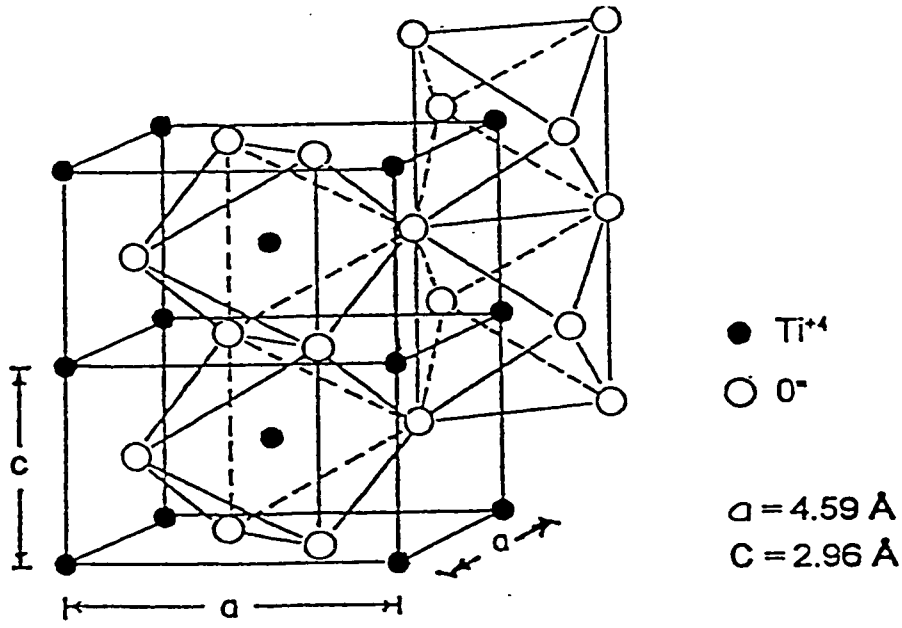

Figure 1.1 The bulk structure of rutile[3].

From figure 1.1, it can be seen that the rutile lattice is the tetragonal structure. The titanium cations are quadruply ionized and the oxygen anions are doubly ionized. The O^{2-} are located at lattice positions of a quasi-perfect octahedral structure while half of these octahedrons are occupied by Ti^{4+} in their centres. The conduction band results from the 3d level of the Ti cations and the valence band comes from the 2p level of the O anions.

Rutile exhibits a predominately (110) natural growth surface. Figure 1.2 shows the structure of the rutile (1×1)(110) surface which is the most stable of the low-index faces. After the surface is polished, bombarded by an argon ion beam, and annealed below 1100K, it still keeps the (1×1) structure, as observed by LEED patterns. As a result, many researchers were interested in investigating the (110) rutile surface. Here, we used a rutile sample coming from a commercially grown single crystal which was sawn and polished along the (110) crystalline plane.

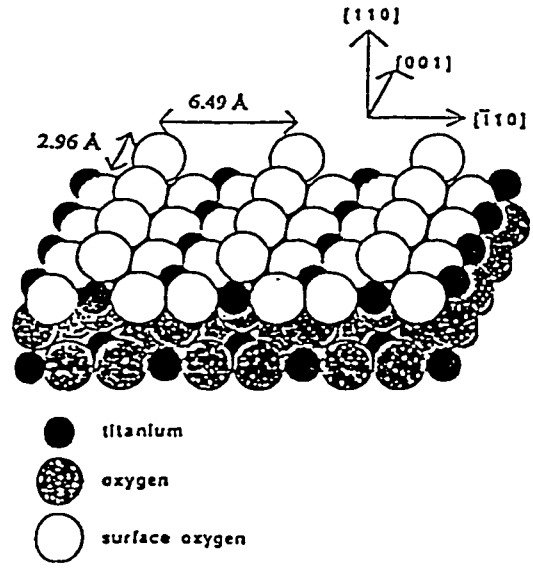

Figure 1.2 Structure of the rutile (1×1)(110) surface[3].

The surface structure may be determined by LEED. Figure 1.3 indicates the diffraction pattern of rutile (1×1) structure. The surface structure may be changed when the sample is annealed at 1150K or above for a while[23], resulting in a (2×1) surface reconstruction.

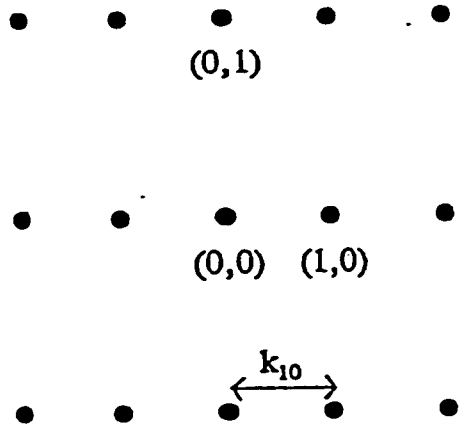

Figure 1.3 The diffraction pattern of LEED from the (1×1)(110) surface[3].

In some sense, the (110) surface is not of a flat surface since there are bridging oxygen atoms at the surface (see figure 1.2). The larger white spheres represent oxygen while the smaller black spheres indicate titanium. The bridging oxygen atoms possess two-fold coordination. In the plane, oxygen atoms are three-fold coordinated. The titanium atoms of the surface connecting with bridging oxygen have six-fold coordination, while those without have five-fold coordination.

In this thesis, Chapter 2 will introduce the theory of low energy electron diffraction, its application to determine surface morphology, and instrumental response. Chapter 3 will describe the experimental methods including sample preparation, creation of ultrahigh vacuum and measurements of diffraction spot profiles. Chapter 4 will give the experimental results and analysis for the flattening exponent, the terrace height distribution, and the interface width. After that, Chapter 5 will carry out the discussion of the experimental results and Chapter 6 will give our conclusions.

Chapter 2. Theory of Low Energy Electron Diffraction

In this chapter we deal in some detail with scattered electron waves from ion cores at a crystalline surface and give the some basic concepts of lattices and reciprocal lattices. Then, we further discuss diffraction conditions and diffraction intensities from a TiO_2 perfect crystalline surface and a stepped homogenous crystalline surface. Finally we discuss the instrumental response.

2.1 Low Energy Electron Diffraction

The low energy electron waves interact with ion cores at a crystalline surface to produce diffraction patterns. This process is called low energy electron diffraction or LEED. As early as 1927, Davisson and Germer discovered the LEED phenomenon at a crystal of nickel[25]. It was not until about the 1960's that the LEED method was extensively applied in research of surface crystallography after the development of ultrahigh vacuum technology, contamination-free electron guns and progress in sample preparation. Unlike X-ray diffraction from crystals, LEED mainly results from the first few atomic layers on a crystalline surface since the electron waves with energy 10-1000 eV can penetrate

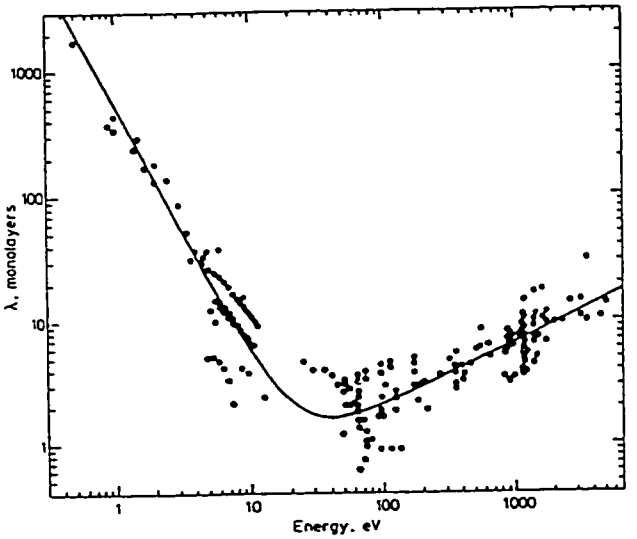

Figure 2.1. Average free paths of electrons as a function of energy[25].

a maximum average free path of about a few monolayers(see figure 2.1) without inelastic scattering, while X-rays possess a much larger depth of penetration than the low energy electron waves. As a result, the LEED method is the most suitable for investigation of crystalline surfaces. It is not only used to investigate the crystallographic structure of a perfect, flat surface, but also to analyze surface defects including surface steps and surface impurities.

2.1.1 Scattering and Scattering Intensity

Before introducing the principles of LEED we need to discuss the scattering of a plane electron wave at a crystalline surface since diffraction is a result of elastic scattering. At first, let us consider a plane electron wave to be scattered by an ion core since the valence electrons in an atom contribute rather little to the scattering process[38]. We assume $\exp(i\mathbf{k}_0\cdot\mathbf{r})$ as the incident plane electron wave. $\mathbf{k}_0$ is the incident electron wave vector with a magnitude of $2\pi/\lambda$, where λ is the wavelength of the electron wave and is related to the electron energy. $\mathbf{r}$ indicates the distance at some point away from the center of the ion core. The scattered electron wave radiates from the ion core (see figure 2.2a). $\mathbf{k}_s$ is the scattered wave vector and θ^s is the scattering angle between the incident wave vector and the scattered wave vector. If the electron wave is scattered elastically, $k_0=k_s$. The total wave function at the distance $\mathbf{r}$ may be expressed by[39]

$$\Psi(\vec{r},\vec{k}_0,\vec{k}_s) = e^{i\vec{k}_0\cdot\vec{r}} + f(\theta^s)\frac{e^{ik_s r}}{r}, \qquad (2\text{-}1)$$

where $f(\theta^s)$ is the dynamic scattering factor of the ion core as a function of θ^s. $k_s r$ describes the phase of the scattered electron wave. The factor 1/r is due to the spreading of the scattered spherical wave. Our discussion above referred to the simple situation in which the reference point is set at the central position of the ion core. In an actual situation, there are many ion cores at a crystalline surface so that it is impossible for us to set every ion core at the origin. Therefore, we need further to consider an ion-core position as ρ with respect to a reference point O (see figure 2.2b). The phase of the spherical wave

at the point P will be changed into $i(\mathbf{k}_0\cdot\rho+k_s r)$. In addition, in our actual measurements, the size of the electron beam diameter is much smaller than the distance between the point P and the ion core so that the effect of the incident electron wave at the point P may be ignored. Eq.(2-1) may approximately be rewritten as

$$\Psi(\vec{r},\vec{k}_0,\vec{k}_s)\approx f(\theta^s)\frac{e^{i(\vec{k}_0\cdot\vec{\rho}+k_s r)}}{r}. \qquad (2\text{-}2)$$

From Eq.(2-2) it can be seen that the wave function mainly comes from the scattered spherical waves at the P point. Now, we further consider the experimental geometry in figure 2.2b. Generally speaking, the detector is placed very far away from the ion core and the reference point is in the vicinity of the ion core. As a result, we can take $R \gg \rho$ and $r \approx R-\rho\cos\theta$. The phase of Eq. (2-2) can be approximately written as

$$i(\vec{k}_0\cdot\vec{\rho}+k_s r)\approx i(\vec{k}_0\cdot\vec{\rho}-k_s\rho\cos\theta)+ik_s R,$$

where R is the distance between the reference point and the detector. Since the directions of **R** and **r** are approximately the same looking from the detector, the factor on the right hand side of the above equation can be rewritten as[5]

$$i(\vec{k}_0\cdot\vec{\rho}-k_s\rho\cos\theta)\approx i(\vec{k}_0-\vec{k}_s)\cdot\vec{\rho}.$$

Here, we define $\mathbf{k}=\mathbf{k}_s-\mathbf{k}_0$ as the momentum transfer vector in the scattering process. The scattered spherical wave of Eq.(2-2) may be approximately expressed by

$$\Psi(\vec{\rho},\vec{k}_0,\vec{k}_s)\approx f(\theta^s)\frac{e^{ik_s R}e^{-i\vec{k}\cdot\vec{\rho}}}{R}. \qquad (2\text{-}3)$$

During measurements, we are only interested in the relative intensity of the scattered waves so that we can ignore the constant attenuation factor 1/R and the constant phase factor $\exp(ik_s R)$. The relative amplitude of the scattered spherical wave from the ion core can be written as

$$A(\vec{\rho},\vec{k}_0,\vec{k}_s) = f(\theta_n^s)e^{-i\vec{k}\cdot\vec{\rho}}. \qquad (2\text{-}4)$$

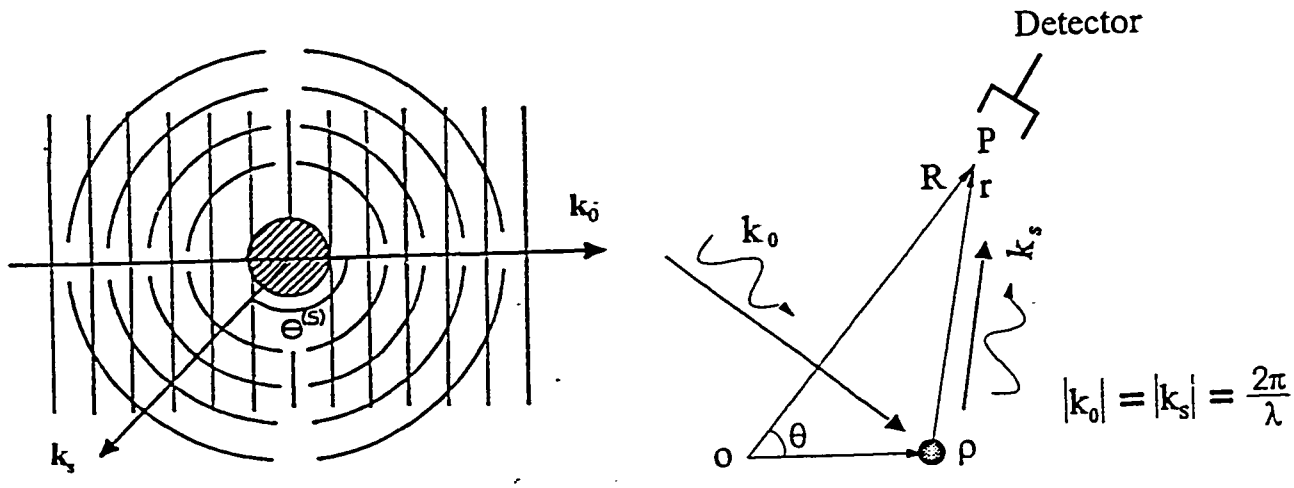

Figure 2.2. The plane electron waves are scattered by an ion core. a) An ion-core immersed in plane electron waves[39]. b) The detection of the scattered wave[5].

If we consider single scattering from ion cores at the crystalline surface only, the total relative scattering amplitude is the sum of the amplitudes produced by every ion core and may be written as

$$A(\vec{k}_0,\vec{k}_s) = \sum_n f(\theta_n^s)e^{-i\vec{k}\cdot\vec{\rho}_n}. \qquad (2\text{-}5)$$

From experimental measurements, it is impossible for us to measure the total scattering wave amplitude and phase since we can measure the scattering intensity only. Based on Eq. (2-5), the scattering intensity at a surface may be expressed by[40]

$$S(\vec{k}_0,\vec{k}_s) = \sum_m \sum_n f(\theta_n^s)f^*(\theta_m^s)e^{-i\vec{k}\cdot(\vec{\rho}_n-\vec{\rho}_m)}. \qquad (2\text{-}6)$$

Eq.(2-6) gives the scattering intensity from single scattering only. However, in our actual measurements, the scattering intensity is due to not only single scattering but also multiple scattering.

That is, the plane electron wave might interact with several ion cores one by one and produce multiple scattering. Because the process of multiple scattering is more complicated, it is very difficult to express in a simple mathematical formula. Luckily, multiple scattering extends over smaller areas in comparison with terrace areas at a surface so that the intensity due to multiple scattering changes slowly over the typical width of a spot profile. As a result, multiple scattering may be included approximately in the dynamic form factor(F(p) in Eq.(2-18)). So, when studying the relative weight, $G_0(k_\perp)$, of the Bragg peak, we do not need to analyze the effect of multiple scattering.

2.1.2 Lattice and Reciprocal Lattice

In order to understand LEED patterns well, we need to introduce the concepts of lattices and reciprocal lattices since they have a close relationship with diffraction patterns. Lattices are used to describe crystal periodicity. A lattice is defined as the simplest arrangement of points which are arranged in real space with the fundamental periodicity of the crystal. These lattice points need not correspond to actual atomic centers and may represent atoms or unit cells. In a real two-dimensional crystalline surface, the lattice can be expressed by two primitive vectors $\mathbf{a}_1$ and $\mathbf{a}_2$. Also, a reciprocal lattice can be used to describe the periodicity of a given lattice in reciprocal space. The reciprocal lattice can be expressed by two primitive vectors $\mathbf{a}^*_1$ and $\mathbf{a}^*_2$ which can be constructed based on the primitive lattice vectors $\mathbf{a}_1$ and $\mathbf{a}_2$. The relationship between the reciprocal lattice vectors and real lattice vectors is defined as

$$\begin{aligned} \vec{a}_1^* &= 2\pi\frac{\vec{a}_2 \times \vec{n}}{A}, \\ \vec{a}_2^* &= 2\pi\frac{\vec{a}_1 \times \vec{n}}{A}, \\ A &= \vec{a}_1 \cdot (\vec{a}_2 \times \vec{n}), \end{aligned} \qquad (2\text{-}7)$$

where **n** is the unit vector normal to the surface and A indicates the unit area of the real lattice. In order to help understand the relationship between the real lattice and its reciprocal lattice, see figure 2.3 in which the black points show a given oblique real lattice. Based on this real lattice, the reciprocal lattice can be calculated by using Eq.(2-7) and is shown by open circles. What is the reciprocal lattice? From literary meaning, the reciprocal lattice is the inverse of the real lattice. If we use nanometers (nm) as the unit of the real lattice, the unit of its reciprocal lattice will be derived as 1/(nm) which is similar to the unit of momentum($p=\hbar k$). As a result, we can say that the reciprocal lattice corresponds to momentum space. We will further show that the diffraction pattern produced by a real lattice corresponds to its reciprocal lattice. Therefore, reciprocal lattices are a very useful tool for analyzing surface crystallography.

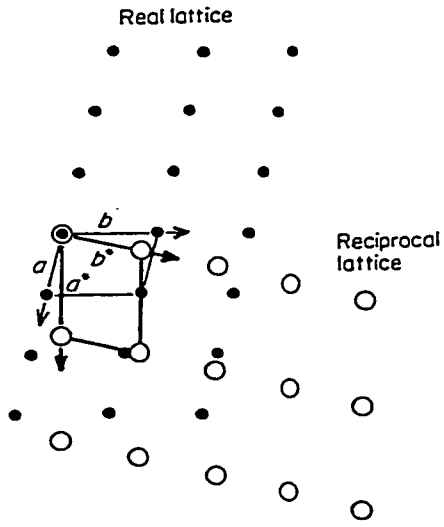

Figure 2.3. An oblique real lattice and its reciprocal lattice[38].

2.1.3 Principles of LEED

As discussed in section 2.1.1, we know that as long as incident plane waves interact with ion cores at a crystalline surface, scattered waves are produced. The elastically scattered waves interfere

to produce a diffraction pattern. The key condition for observing a diffraction pattern is that the wavelength of the incident plane waves must be of the same order of magnitude as the lattice constant of the crystalline surface or be smaller than it. Otherwise, the diffraction pattern does not occur. For example, this is why we have never seen that a diffraction pattern produced by an optical laser on a perfect single crystal surface since the laser wavelength is much longer than the lattice constant of the single crystal. However, X-rays can produce a diffraction pattern from a single crystal because the X-ray wavelength is similar to the atomic lattice constant of the crystal. The wavelength of low energy electrons also meets the requirement for diffraction since the low energy electrons are in a range of 50eV to 1000eV which corresponds the wavelengths of 1.37Å- 0.39Å, comparable to the lattice constant of typical crystals.

Now we consider that incident low energy electron waves from an electron gun interact with ion cores at a crystalline surface and are scattered by the ion cores (see figure 2.4). Since the distance between the electron gun and the crystalline surface is much larger than the size of the electron beam diameter, the incident electron waves may be approximately considered as plane waves so that we

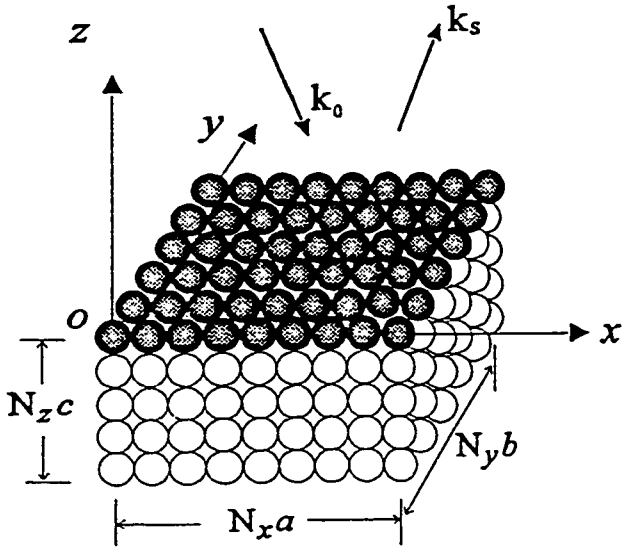

Figure 2.4 Incident electron waves and scattered electron waves on ion cores[5].

can use Eq.(2-6) to determine the diffraction conditions and to calculate the diffraction intensity. According to the two-dimensional Laue condition, diffraction at a crystalline surface must obey

$$\vec{K}_{//} \cdot \vec{a}_1 = 2\pi l, \qquad \vec{K}_{//} \cdot \vec{a}_2 = 2\pi h, \tag{2-8}$$

where $\mathbf{K}_{//}$ is the momentum transfer vector parallel to the surface and l and h are integers. A reciprocal lattice vector $\mathbf{g}_{lh}$ can be expressed by

$$\vec{g}_{lh} = l\vec{a}_1^{*} + h\vec{a}_2^{*}, \tag{2-9}$$

where $\mathbf{a}^*_1$ and $\mathbf{a}^*_2$ are the reciprocal lattice unit vectors. By means of Eq.(2-8) and Eq.(2-9), we can derive

$$\vec{K}_{//} = \vec{g}_{lh}. \tag{2-10}$$

Eq.(2-10) tells us that, on a two-dimensional crystalline surface, the diffraction intensity reaches a maximum only when the momentum transfer vector parallel to the surface equals a reciprocal lattice vector. This means that the diffraction pattern corresponds to the reciprocal lattice.

Equivalently, the wave vectors $\mathbf{k}_s$ of diffraction beams must satisfy the Ewald sphere construction. In order to understand this easily, we consider Ewald sphere construction for a one-dimensional surface shown in figure 2.5. In the figure, the Ewald sphere is drawn as a circle whose radius is given by the magnitude of the incident wave vector $\mathbf{k}_0$. Any scattered wave vector $\mathbf{k}_s$ on this circle satisfies conservation of energy. When the circle intersects with a reciprocal lattice rod, the Laue diffraction condition is also satisfied. As a result, diffraction spots will be observed only for scattered wave vectors for which the Ewald sphere crosses a reciprocal lattice rod.

As the energy of the incident electron waves is increased, the Ewald sphere radius will also increase so that the number of observed diffraction spots increases correspondingly. The result shows that the number of diffraction spots depends on the energy of the incident electrons. In addition,

with increasing electron energy, the intensity of each diffraction spot will change even though the incident electron waves are scattered by a flat crystalline surface. The change of diffraction intensity called the I/V curve (see figure 2.6) mainly results from the interference of electron waves

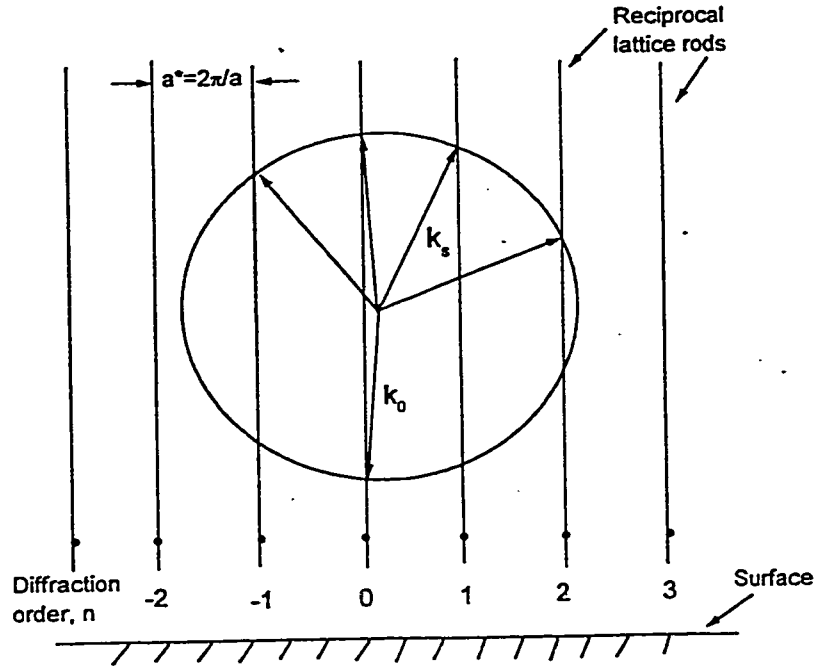

Figure 2.5 The Ewald sphere construction for a one-dimensional surface.

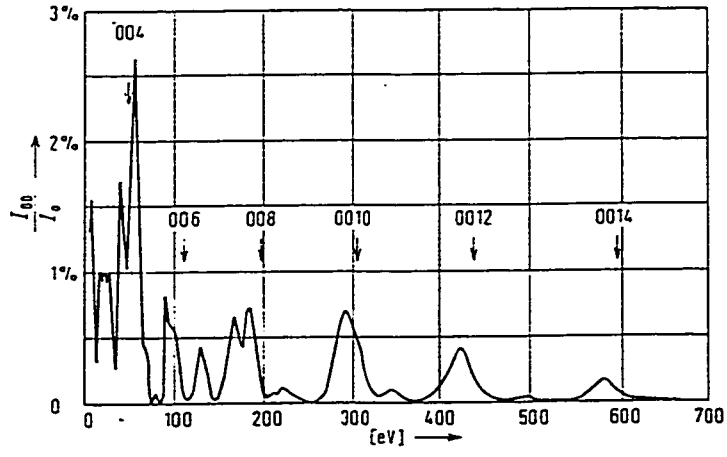

Figure 2.6. Intensity/energy(I/V)-curve for the (0,0)-beam of a clean Ni(100) surface at normal incidence. From Christmann et al[25].

scattered by different ion cores at the crystal surface. The scattering factor, $f(\theta^s)$, depends on not only the scattering angle, θ^s, but also on the incident electron energy, E. This result further tells us that we cannot directly extract information on surface morphology by analyzing and comparing the changes of the absolute diffraction intensity of the Bragg peak delta function at different incident electron energies. However, we can compare the change of the relative weight, $G_0(k_\perp)$, of the Bragg peak delta function to extract the surface information. We will discuss this in detail later.

In the above discussion, we analyzed the scattering intensity from ion cores which were all of the same type and gave a general formula for the scattering intensity (see Eq.(2-6)). Now, we further discuss our sample which is composed of Ti and O elements. We are able to treat this situation in a similar way although the ion cores of Ti and O have different scattering factors. We can consider the unit cell column of TiO_2 perpendicular to the surface. The scattering factor of this column is denoted as $f_n(\mathbf{p})$. For a crystalline surface containing different atoms, the diffraction intensity may still be expressed by

$$S(\vec{k}_0, \vec{k}_s) = \sum_m \sum_n f_n(\vec{p}) f_m^*(\vec{p}) e^{i\vec{k}\cdot(\vec{\rho}_n - \vec{\rho}_m)}, \qquad (2\text{-}11)$$

where $\mathbf{p}$ indicates $(\mathbf{k}_0, \mathbf{k}_s)$ and n indicates the n^{th} unit cell column at the surface. ρ_n indicates the position of the n^{th} unit cell column. Although Eq.(2-11) has a similar form to Eq.(2-6), from a physical point of view, it possesses more general meaning. Later, we will use Eq.(2-11) to calculate diffraction intensity.

2.2 LEED from a Perfect Crystalline Surface

In the previous section, we discussed the principles of LEED and its diffraction intensity. In this section, we concretely analyze the LEED intensity from a TiO_2 perfect crystalline surface. At first, let us suppose that the scattering factor of the unit cell column is approximately constant, that is $f_n(\mathbf{p}) \approx f$. Using Eq.(2-11) we can derive the following diffraction intensity from a perfect surface [5]

$$S(\bar{k}_0, \bar{K}_{//}) = |f|^2 \frac{\sin^2(N_x \bar{K}_{//} \cdot \bar{a}_1) \sin^2(N_y \bar{K}_{//} \cdot \bar{a}_2)}{\sin^2(\bar{K}_{//} \cdot \bar{a}_1) \sin^2(\bar{K}_{//} \cdot \bar{a}_2)}, \qquad (2\text{-}12)$$

where the size of the sample is given by N_x and N_y which are the numbers of unit cells along x and y directions, respectively. $\mathbf{a}_1$ and $\mathbf{a}_2$ are primitive lattice vectors. Eq.(2-12) looks like a delta function when N_x and N_y approach very large numbers. However, in our actual measurements, even though at an in-phase condition, diffraction spot profiles possess some width broadened by the instrumental response.

2.3 LEED from a Stepped Homogeneous Crystalline Surface

In the previous section, we showed the diffraction intensity from a perfect crystalline surface. In this section, we will study the LEED intensity from a TiO_2 stepped homogeneous surface(see figure 2.7). From figure 2.7, we can see that there are two different column types at the stepped surface. By means of Eq.(2-11), the diffraction intensity from the stepped surface may be derived as[40](see Appendix 1)

$$S(\vec{k}_0, \vec{k}_s) = |f(\vec{p})|^2 \sum_n \sum_m e^{-iK_x a_1 (s_n - s_m)/4} e^{-i\vec{k} \cdot (\vec{\rho}_n - \vec{\rho}_m)}, \qquad (2\text{-}13)$$

where $|f(\mathbf{p})|^2$ is the dynamic form factor and is simply denoted as F(p). s_n depends on column types (its value: 1 or -1). The momentum transfer vector $\mathbf{k}$ may be split into $\mathbf{k}_\perp$ perpendicular and $\mathbf{K}_{//}$ parallel to the surface, that is $\mathbf{k}= \mathbf{k}_\perp+\mathbf{K}_{//}$. The position of one unit cell column may be indicated as

$$\vec{\rho}_n = \vec{r}_n + h(\vec{n})\vec{d}, \qquad (2\text{-}14)$$

where $\mathbf{r}_n$ is the distance parallel to the crystal surface and h($\mathbf{n}$) is an integer. $\mathbf{d}$ is perpendicular to the crystal surface with magnitude equal to the step height. We insert Eq.(2-14) into Eq.(2-13) which will be changed to

From Eq.(2-15), it can be seen that the diffraction intensity is influenced by three phase factors: The first and the second phase factors come from the effect of the terrace height distribution and the third term is the effect of the positions of unit cell columns. If the surface height keeps constant (h(**n**)=h(**m**)), the diffraction intensity is the same as that from a perfect surface discussed in section 2.2. If the height at the surface changes with column position (h(**n**)≠h(**m**)), the diffraction intensity of the

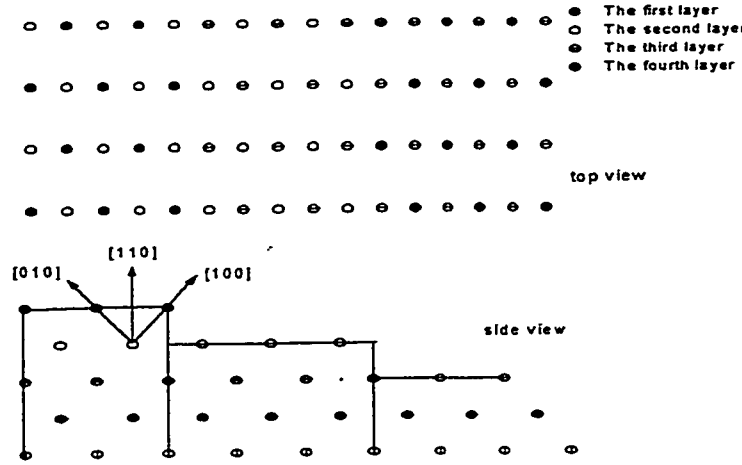

Figure 2.7 The structure of a stepped (110) TiO_2 surface as seen from a top view and a side view showing Ti atoms only.

Bragg peak will be reduced due to destructive interference and, at the same time, the interference causes a diffuse shoulder profile. In order to make the study of the surface simpler, we choose the (0,0) diffraction spot and let $\mathbf{n} - \mathbf{m} = \mathbf{l}$ and $\mathbf{r}_n - \mathbf{r}_m = \mathbf{r}_l$. The phase of the first term is a very small amount for $K_{//}$ near $G_{(0,0)}$. Therefore, it may be neglected. Eq. (2-15) may be simplified to

$$S(\vec{k}_0, \vec{k}_s) = NF(p)\sum_l \left\langle e^{idk_\perp(h(\vec{m}+\vec{l})-h(\vec{m}))} \right\rangle e^{\vec{K}_{//}\cdot\vec{r}_l}, \qquad (2\text{-}16)$$

where the brackets <> denote averaging with respect to **m**, that is

where the brackets <> denote averaging with respect to **m**, that is

$$\left\langle e^{idk_{\perp}(h(\vec{m}+\vec{l})-h(\vec{m}))} \right\rangle = \frac{\sum_{m} e^{idk_{\perp}(h(\vec{m}+\vec{l})-h(\vec{m}))}}{N}, \qquad (2\text{-}17)$$

where N are the number of unit cell columns at the crystalline surface. Eq.(2-16) describes the diffraction intensity of the (0,0) spot from a TiO_2 stepped homogenous (110) surface and may be simply denoted as

$$S(\vec{k}_0, \vec{k}_s) = NF(p)G(k_{\perp}, \vec{K}_{//}), \qquad (2\text{-}18)$$

where $G(k_{\perp}, \mathbf{K}_{//})$ is defined as the surface structure factor which is expressed by

$$G(\vec{k}_{\perp}, \vec{K}_{//}) = \sum_{l} \left\langle e^{idk_{\perp}(h(\vec{m}+\vec{l})-h(\vec{m}))} \right\rangle e^{i\vec{K}_{//}\cdot\vec{r}_l}. \qquad (2\text{-}19)$$

From Eq.(2-18), it can be seen that the diffraction intensity is the product of the dynamic form factor and the surface structure factor. Since we have introduced the dynamic form factor in previous sections, we now will focus on discussing the structure factor. The structure factor contains information on the surface morphology such as the surface terrace height distribution, average terrace width and surface defects. As a result, we may extract the surface information by analyzing the structure factor. In our actual measurements, we can measure diffraction intensity, but we cannot directly determine the structure factor $G(k_{\perp}, \mathbf{K}_{//})$ since the form factor F(p) is variable and also unknown. However, we can determine the relative size of the structure factor $G(k_{\perp}, \mathbf{K}_{//})$ from spot profiles since the structure factor $G(k_{\perp}, \mathbf{K}_{//})$ may be split into both the Bragg peak from the instrumental response and the diffuse shoulder profile from the terrace height distribution and is expressed by[22]

$$G(k_{\perp}, \vec{K}_{//}) = G_S(k_{\perp}, \vec{K}_{//}) + G_{diff}(k_{\perp}, \vec{K}_{//}), \qquad (2\text{-}20)$$

where $G_\delta(\mathbf{k}) = G_0(k_\perp)G_{ideal}(\mathbf{K}_{//})$ and $G_0(k_\perp)$ is the relative weight of the Bragg peak delta function. Based on Eq.(2-20), we may derive a new relationship as (see Appendix 2)

$$G(k_\perp, \vec{K}_{//}) = G_0(k_\perp)G_{ideal}(\vec{K}_{//}) + (1 - G_0(k_\perp))\Phi(k_\perp, \vec{K}_{//}), \qquad (2\text{-}21)$$

where $\Phi(k_\perp, \mathbf{K}_{//}) = A_{BZ}S_{diff}(k_\perp, \mathbf{K}_{//})/\int S_{diff}(k_\perp, \mathbf{K}_{//})d\mathbf{K}_{//}$ is the effect of surface terrace widths and A_{BZ} is the area of the surface Brillouin Zone(BZ). From Eq.(2-21) it can be seen that when $G_0(k_\perp)=1$, $G(k_\perp, \mathbf{K}_{//}) = G_{ideal}(\mathbf{K}_{//})$. This is an in-phase condition. The in-phase condition is defined as $k_\perp d = 2\pi n$, where n is an integer. If the $G_0(k_\perp)$ value reduces, the Bragg peak intensity lowers while the diffuse intensity increases. The relative weight, $G_0(k_\perp)$, of the Bragg peak contains information on the terrace height distribution at the surface and can be expressed by (see Appendix 3)

$$G_0(k_\perp) = \sum_h C_h \cos(dk_\perp h), \qquad (2\text{-}22)$$

where $C_h = \Sigma P_l P_{l+h}$. P_l indicates the fraction of the surface that is at height l. As such, the surface analysis becomes simpler since we only need to analyze the relative weight $G_0(k_\perp)$, instead of the structure factor $G(k_\perp, \mathbf{K}_{//})$, to extract the information on P_l. The relative weight $G_0(k_\perp)$ can be easily determined experimentally since it can be expressed as the ratio of the integrated Bragg peak intensity to the total integrated diffraction intensity(see Appendix 4)

$$G_0 = \frac{\iint_{B.Z} S_\delta(k_\perp; \vec{K}_{//})d^2K_{//}}{\iint_{B.Z} S(k_\perp; \vec{K})d^2K_{//}}. \qquad (2\text{-}23)$$

In terms of Eq.(2-23), if we want to determine the values of the relative weight $G_0(k_\perp)$, we need to separate the Bragg peak and diffuse profile from the measured spot profile and calculate the

integrated Bragg peak intensity and the total integrated intensity. After getting the relative weight $G_0(k_\perp)$ varying with $k_\perp$, we may use Eq.(2-22) to determine the terrace height distribution. In addition, from the diffuse shoulder at the out-of-phase condition, we can determine the full width at half maximum(FWHM). Based on the size of the FWHM, the average terrace width, l, at the surface can be determined according to definition as follows

$$l = \frac{4}{FWHM} . \qquad (2\text{-}24)$$

Based on the terrace height distribution, we may further determine the interface width defined as

$$w^2 = \left\langle (h - \langle h \rangle)^2 \right\rangle, \qquad (2\text{-}25)$$

where h and <h> are the surface height and the average surface height, respectively. The bigger the value of the interface width is, the rougher the surface is.

2.4 Instrumental Response and Resolution

In previous sections, we mainly focussed on discussing surface characteristics and analyzing the diffraction intensity at a TiO_2 surface. In this section, we will discuss the instrumental response.

It is well known that, even for a perfect crystal having an infinitely large surface, we would not observe a delta function for the diffraction spot profile in our actual measurements. This is because instruments have their responses which broaden the width of spot profiles measured. The width comes from instrumental effects such as detector aperture size, electron energy spread, electron beam divergence and so on (see Appendix 5). In order to understand the instrumental response clearly, let us assume that $T_i(\mathbf{k}-\mathbf{k}_0)$ and $T_f(\mathbf{k}', \mathbf{K}'_{//}-\mathbf{K}_{f//})$ are the distribution of $\mathbf{k}$ vectors of incident electrons and the response of the detector, respectively. The wave vector $\mathbf{k}$ refers to the incident electron wave and is expressed as $(k^z, \mathbf{K}_{//})$, where the vector $\mathbf{K}_{//}$ and k^z are parallel and vertical to the crystalline surface, respectively. The wave vector $\mathbf{k}'$ is the scattered electron wave vector in space. Let us further suppose

that S(**k'**, **k**) is the surface response function which can be expressed as S(**k**, **K'**$_{//}$-**K**$_{//}$). As a result, the total intensity from the effect of the instrument and a crystalline surface may be expressed by[40]

$$I(\bar{k}_f, \bar{k}_0) = \iiint d^2K_{//} d^2K'_{//} dk^z T(k'; \bar{K}_{f//} - \bar{K}'_{//}) S(\bar{k}; \bar{K}'_{//} - \bar{K}_{//}) T_i(\bar{k} - \bar{k}_0), \quad (2\text{-}26)$$

where $T_i(\mathbf{k}-\mathbf{k}_0)=T_i(\mathbf{k}^z-\mathbf{k}^z_0; \mathbf{K}_{//}-\mathbf{K}_{//0})$. If we only consider elastically scattered waves, then k'=k. In addition, for a narrow distribution of incident electron wave vectors, we may assume that $k \cong k_0$ and $\mathbf{k} \approx \mathbf{k}_0$. Eq.(2-26) can be rewritten as

$$I(\bar{k}_f, \bar{k}_0) = \iint d^2K_{//} d^2K'_{//} T(k_0; \bar{K}_{f//} - \bar{K}'_{//}) S(\bar{k}_0; \bar{K}'_{//} - \bar{K}_{//}) T_i(\bar{k}_0; \bar{K}_{//} - \bar{K}_{0//}), \quad (2\text{-}27)$$

where $T_i(\mathbf{k}_0; \mathbf{K}_{//}-\mathbf{K}_{//0})=\int d\,k^z\, T_i(\mathbf{k}^z-\mathbf{k}^z_0; \mathbf{K}_{//}-\mathbf{K}_{//0})$. If we suppose that the crystalline surface is perfect, then $S(\mathbf{k}_0, \mathbf{K}'_{//}-\mathbf{K}_{//}) \propto \delta(\mathbf{K}'_{//}-\mathbf{K}_{//})$. Eq.(2-27) may further be simplified to

$$I(\bar{k}_f; \bar{k}_0) \propto \int d^2K'_{//} T(k_0; \bar{K}_{f//} - \bar{K}'_{//}) T_i(\bar{k}_0; \bar{K}'_{//} - \bar{K}_{0//}). \quad (2\text{-}28)$$

From Eq.(2-28), it can obviously be seen that, under the condition of a perfect surface, the width of diffraction spot profiles results from the instrumental effects called instrumental response. If the sample surface is rough, Eq.(2-27) can be transformed to

$$I(\bar{k}_f, \bar{k}_0) = \int d^2K_{//} T(\bar{k}_0; \bar{K}_{f//} - \bar{K}_{//}) S(\bar{k}_0; \bar{K}_{//} - \bar{K}_{0//}), \quad (2\text{-}29)$$

where $T(k_0 ; \mathbf{K}_{f//}-\mathbf{K}_{//})=\int d^2K'_{//} T_f(k_0; \mathbf{K}_{f//}-\mathbf{K}'_{//}) T_i(\mathbf{k}_0; \mathbf{K}'_{//}-\mathbf{K}_{//})$. Eq.(2-29) further tells us that for a rough surface the diffraction intensity depends on the convolution of the instrumental response and the surface response function, which makes the investigation complicated. Fortunately, at an in-phase condition, if there are no other defects on the surface besides steps, the rough surface response function $S(\mathbf{k}_0; \mathbf{K}_{//}-\mathbf{K}_{0//})$ is proportional to $\delta(\mathbf{K}_{//}-\mathbf{K}_{0//})$. The equation (2-29) at the in-phase condition is changed to

$$I(\bar{k}_f; \bar{k}_0) \propto T(k_0; \bar{K}_{f//} - \bar{K}_{0//}). \quad (2\text{-}30)$$

Eq.(2-28) and Eq.(2-30) are the exact same. From the result, we know no matter whether a surface is perfect or rough, at an in-phase condition, the spot profiles of the diffraction intensity are identical since the instrumental resolution does not change after the instrumental parameters are fixed. We can determine the instrumental resolution by measuring the full-width at half maximum (FWHM) of spot profiles at the in-phase condition. The instrumental transfer width is defined as the inverse of the FWHM and is written as

$$T = \frac{2\pi}{FWHM}. \qquad (2\text{-}31)$$

From Eq.(2-31), it can be deduced that the smaller the FWHM is, the larger the transfer width is. With the larger transfer width, we can analyze a bigger area on a sample surface coherently . So, in order to get more accurate results, we generally try to raise the instrumental transfer width, but each instrument has its limit.

Chapter 3. Experimental Methods

In this chapter, the preparation of a TiO_2 sample and the methods for creating and measuring ultrahigh vacuum pressures are described. After that, we will further introduce the experimental methods of Auger electron spectroscopy (AES) and low energy electron diffraction spot profile analysis(SPA-LEED). In addition, we will briefly describe the argon ion sputtering gun and the temperature controller for sample annealing.

3.1 Sample Preparation

Our rutile sample with a polished (110) surface was cut into a square shape with size 12×12 mm^2 and thickness 0.9 mm. The sample was grooved on two of its edges for glueing thermocouples(chromel- alumel) by using a ceramic adhesive. The sample was mounted beneath a 0.5 mm thick, round molybdenum sample holder with a 10 mm diameter bevelled hole in its centre and fixed by two small clips made of a 0.13 mm thick molybdenum sheet. The sample holder was attached to a sample manipulator by a rigid stainless steel bracket (see figure 3.1). The sample and its holder were connected to ground through an external connector, but isolated from the rest of the sample manipulator assembly. By grounding the sample externally, its charging is prevented and its current can be measured during the SPA-LEED experiments.

Before the manipulator with the sample was installed onto the vacuum chamber equipped with surface analysis instruments, the sample surface, at first, was rinsed by using generous amounts of acetone for removing grease and dusts. Then, methanol was used to rinse the surface. In order to get a cleaner surface, we needed to repeat this process several times until we could not find any trace of solvent residues or other contaminants with our naked eyes or with the help of a magnifying glass. After that, the manipulator with the sample was installed upon the chamber.

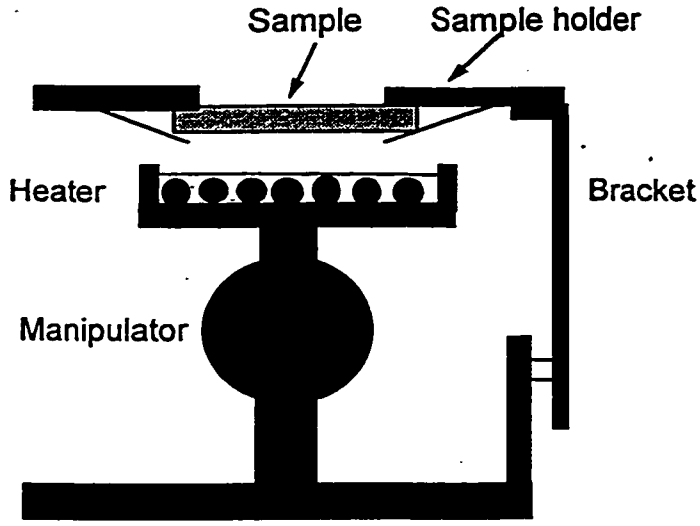

Figure 3.1 A sample and its holder.

Although the sample surface was treated by using acetone and methanol several times, it was still not clean on the microscopic scale due to small amounts of carbon and other impurities adsorbed on it. These impurities at the surface could not be seen by our naked eyes, so we had to use Auger electron spectroscopy to test for them. Therefore, the surface needed to be cleaned further by using argon ion sputtering in ultrahigh vacuum conditions. These methods will be introduced in later sections.

3.2 Ultrahigh Vacuum Chamber

In order to keep the sample surface clean for the period of time needed to make our experimental measurements, it is very necessary for us to produce ultrahigh vacuum conditions reaching the pressure of 10^{-10} Torr or lower. For example, if pressures in the vacuum chamber are at about 10^{-6} Torr, a crystal surface is covered very soon (in a few seconds) by gas from air such as C, H, and N in the chamber. A contaminated surface might influence our experimental results, from which we might obtain incorrect conclusions. In addition, the surface analysis instruments such as AES and

LEED also need high vacuum conditions~10^{-8} Torr. As a result, the study of our crystalline surface had to be carried out in the ultrahigh vacuum chamber which was made of stainless steel with an outside diameter 12"(see figure 3.2). The chamber was equipped with surface analysis instruments such as AES and SPA-LEED and vacuum equipment such as a roughing pump, a turbo-molecular pump, two ion pumps and a titanium sublimation pump.

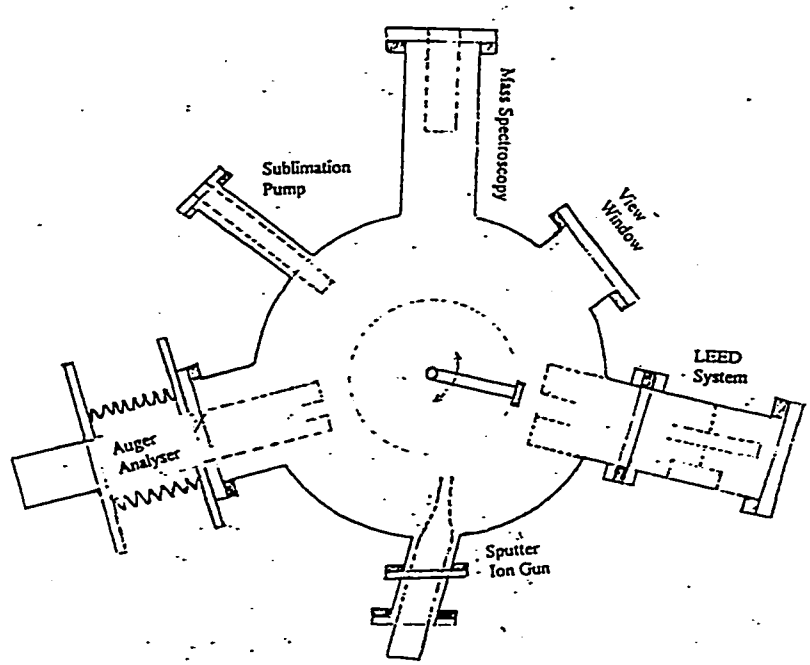

Figure 3.2 A diagram of the vacuum chamber from side view.

How were ultrahigh vacuum conditions produced? Initially, the mechanical pump was used with a pumping speed of 127 L/min to produce a low vacuum pressure after the manipulator with the sample was installed on the conflat flange sealed with an oxygen-free copper gasket. Then, the turbo-molecular pump with a pumping speed of 56 L/s was used to reduce the pressure further to produce a high vacuum. To reach ultrahigh vacuum pressures, pumping alone was not usually sufficient. Accordingly, the vacuum chamber was baked out by heating it uniformly for about 12 hours in the temperature range 130-180°C while the system was pumping. The purpose of this bake-out was to accelerate the outgassing of materials deposited on the inner walls of the chamber and all the

equipment during the last contact with atmospheric pressures. When the chamber was baked out, the pressure in it increased at first due to outgassing of all the inner equipment interfaces and walls. After a longer period of time, the rate of the outgassing became smaller and smaller so that the chamber pressure started lowering. After the bake-out heaters were turned off, the two ion pumps with speeds of 60 L/s and 30 L/s were turned on. During cooling, the chamber pressure decreased to about 10^{-9} Torr. The titanium sublimation pump was used to reduce the chamber pressure further by evaporating a thin titanium film onto the inner surface of the chamber because this film chemically combines with nearly all gases impinging on it except the noble gases. Generally speaking, the whole process to produce an ultrahigh vacuum pressure of 10^{-10} Torr or lower requires two to three days or a little longer.

In the previous paragraph, we described how to produce ultrahigh vacuum conditions, but how were the vacuum chamber pressures measured? For low vacuum pressures, we used a thermocouple gauge to measured them and for high or ultrahigh vacuum pressures we used a Bayard-Alpert ionisation gauge to measure them. Figure 3.3 shows a Bayard-Alpert ionisation gauge.

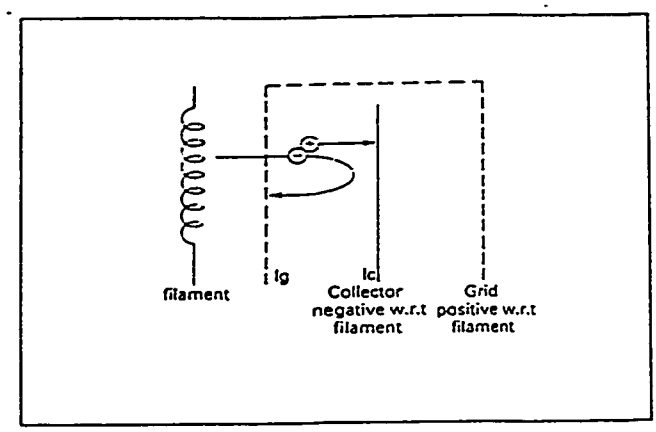

Figure 3.3 A Bayard-Alpert ionisation gauge [41].

From figure 3.3, it can be seen that thermally emitted electrons from the hot filament are

accelerated to the grid and produce a few oscillations through their wires. They are captured by the grid and form current I_g. Before they are captured by the grid, they collide with gas molecules and make the molecules ionized. The ionized gas molecules move to the collector and produce positive ion current I_c. For a given electron emission current I_g, the positive ion current I_c is proportional to the density of gas molecules near the ionisation gauge in the chamber. At the same time, the density of gas molecules is also proportional to the vacuum pressure P. So, the measured collector current I_c may be expressed as

$$I_c = GI_g P, \qquad (3\text{-}1)$$

where G is called the sensitivity constant of the gauge. By measuring the collector current I_c, we can determine the high or ultrahigh vacuum pressures.

3.3 Auger Electron Spectroscopy (AES)

3.3.1 Physical Principles of AES

Auger electron spectroscopy is a powerful technique for analysing the chemical compositions of materials at surfaces based on the Auger electron emission process. The technique takes advantage of the surface sensitivity of low energy electrons (see figure 2.1). That is, the incident electrons with higher energy make core energy levels of atoms at a crystalline surface ionized and then Auger electrons are emitted. Only the Auger electrons from the first few atomic layers at the surface can be detected at the elastic peak energy by the energy analyser, while the Auger electrons from deeper atomic layers are smeared out into the background due to inelastic scattering before leaving the surface.

Now we describe the process of producing an Auger electron in detail. When a beam of incident electrons with energy of 2keV from an electron gun impinges on atoms at a sample surface, an inner-shell electron (E_1) of an atom is kicked off and the atom is left with a hole in its inner-shell (see figure

3.4). Such an atomic state is called an excited one. Since the atom with the excited state is unstable, the de-excitation happens immediately. That is, an electron of a higher energy level (E_2) in the atom transfers to the lower energy level (E_1) and the process will emit a characteristic energy of E_2-E_1 which might generate an X-ray or excite another electron from a nearby bound energy level (E_3) to a free state. The free electron is termed an Auger electron and its kinetic energy E_{ke} is

$$E_{ke} = E_3 + E_2 - E_1 - \Phi. \qquad (3\text{-}2)$$

The Auger electron loses some of its kinetic energy in escaping the potential energy barrier at the sample surface given by the work function Φ. Generally speaking, the work function is typically about 3-5eV. The kinetic energy E_{ke} of the Auger electron is characteristic of three electronic energy levels of the atom. By using an energy analyser to measure the peak of the kinetic energy E_{ke}, we can determine the chemical elements at the sample surface since different atoms have different characteristic energies E_{ke}. From here, we can also see that Auger electron spectroscopy cannot detect light elements such as H and He.

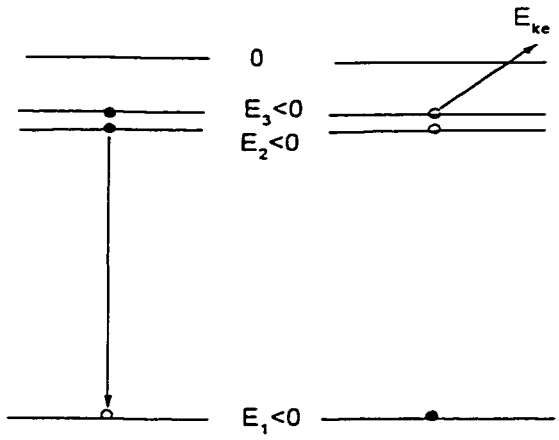

Figure 3.4 The Auger process.

3.3.2 Measurement of AES

The Auger electron spectroscopy instrument is mounted on the ultrahigh vacuum chamber(see

figure3.2). It is composed of an electron gun for sample excitation and a cylindrical mirror analyser (CMA) for detection of Auger electrons. Figure 3.5 shows a schematic diagram of the AES instrument.

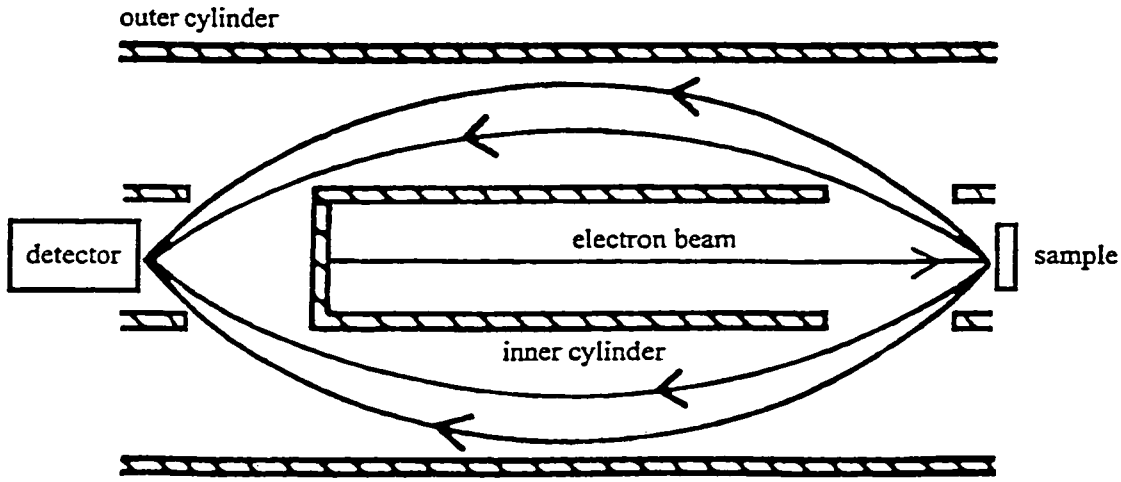

Figure 3.5 A schematic diagram of the AES instrument[3].

From figure 3.5, it can be seen that the CMA is an electrostatic lens system made of two coaxial cylindrical electrodes, which produce an electrostatic field of cylindrical symmetry. The outer cylinder is held at a negative potential with respect to the inner cylinder which is grounded. When a beam of electrons with energy 2 keV from the electron gun impinges on a sample surface, Auger electrons are created and, by selecting the electrostatic field, are focussed to enter exit slits and the detector which records the Auger electron signal N(E). However, in actual measurements for impurities at a surface, the Auger electron peaks are very small in the secondary electron spectrum N(E). In order to see them clearly, one typically uses electronic differentiation to display dN(E)/dE instead of N(E) as a function of Auger electron energy. For example, an Auger electron spectrum is shown in figure 3.6 from which it can be seen that the distribution of Auger electron peaks varying with energy may be divided into three regions. The first region from 220eV to 290eV contains a very small peak which

is at 273eVcorresponding the KLL transition in carbon. In the second region from 330eV to 440eV, there are several peaks at 330eV, 354eV, 364eV, 384eV and 418eV which correspond to the LMM transition in titanium. In the third region of 460eV to 550eV, the peaks at 468eV, 483eV and 503eV show the KLL transition in oxygen.

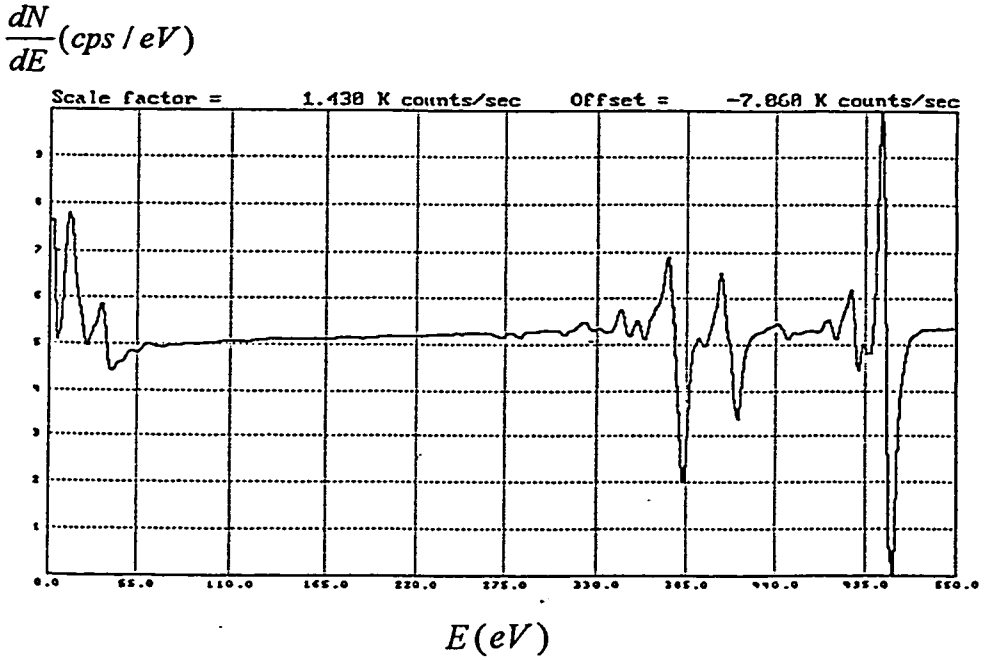

Figure 3.6 An Auger electron spectrum of a measured sample at (110) surface.

3.4 Spot Profile Analysis-LEED (SPA-LEED)

3.4.1 Description of SPA-LEED Instrument

"SPA-LEED" is the abbreviation for low energy electron diffraction spot profile analysis. With this technique, we can observe electron diffraction patterns qualitatively on a phosphor screen or determine the intensity distribution of diffraction spots quantitatively by using a channeltron detector. A computer records the data of the intensity distribution.

The SPA-LEED instrument is composed of an electron gun, deflection plates, focussing lenses, a phosphor screen, retarding grids, and a channeltron (see figure 3.7). The instrument was mounted

on an 8" conflat flange of the vacuum chamber(see figure 3.2). We will further describe the function of each component briefly. Figure 3.8 shows a diagram of the electron gun of the SPA-LEED instrument. Electrons are produced at a heated tungsten filament by thermionic emission. The difference in voltages between the filament and ground potential determines the final kinetic energy gained by the electrons. An "extractor" voltage influences the electron beam by controlling the emission electron current and focussing it somewhat. The Einzel-lens(F1) in the electron gun can be used to focus the electron beam before it leaves for the sample surface.

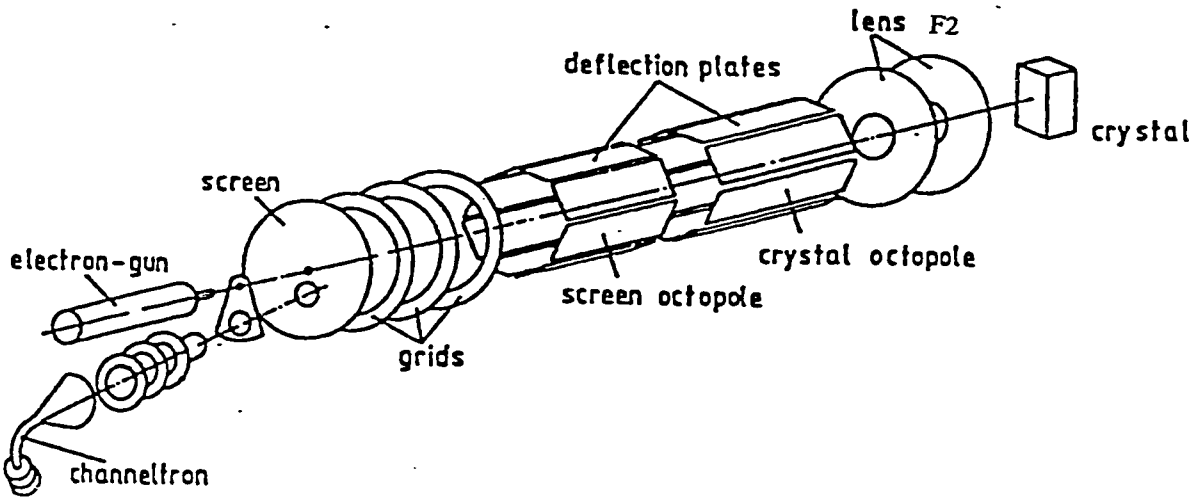

Figure 3.7 A schematic diagram of the SPA-LEED system[41].

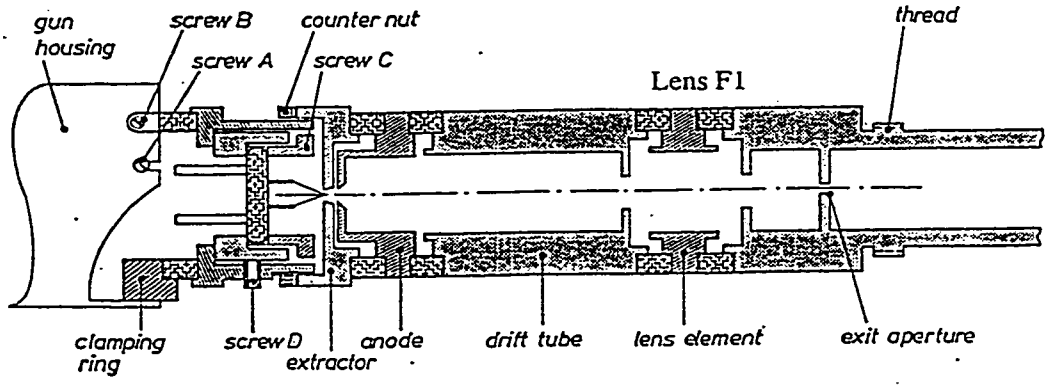

Figure 3.8 A schematic diagram of the electron gun of SPA-LEED[41].

To obtain higher resolution, we mainly used the second lens (crystal lens labeled F2) in front of the sample instead(see figure 3.7). It focusses a divergent electron beam from the electron gun to be parallel when incident on the sample surface, and then focusses the diffraction electron beam onto the channeltron detector or the screen. This second lens lets the SPA-LEED instrument obtain high resolution. Between the crystal lens and the screen with grids, there are two octopoles which are used for the deflection of the electrons. In comparison with scanning with four deflection plates, the octopoles provide better field homogeneity. The channeltron is an electron detector which counts pulse signals up to rates of 10^6 counts per second(cps). The diffracted electrons enter the channeltron housing through an aperture of 100μm diameter.

3.4.2 The Measurement of SPA-LEED on a Sample Surface

In the previous section, we briefly described the SPA-LEED instrument. In this section, we will describe how to use it to carry out measurements on a sample surface. At first, we suppose that the sample has been installed properly into the chamber whose pressure reaches an ultrahigh vacuum condition and that the sample has also been cleaned by using argon ion bombardment and then annealed. After that, we could perform our experiment. We needed, at first, to check the diffraction pattern qualitatively on the phosphor screen. We focussed the electron beam by adjusting the two electrostatic lenses, and then observed the diffraction pattern on the screen for different electron energies. After observing the diffraction pattern on the screen, only then did we continue to make the SPA-LEED measurements.

The SPA-LEED apparatus was controlled by commercially-made software which could perform one-dimensional and two-dimensional scans of the diffraction pattern. Generally speaking, we used the two-dimensional scanning mode to determine the position of deflection voltages of the (0,0) diffraction spot on the computer screen. Then, by using one-dimensional scans and adjusting LEED parameters, the focus was adjusted to reduce the full width at half maximum (FWHM) of the (0,0)

diffraction spot profile to reach a minimum, at an in-phase condition. By analysing the FWHM at an in-phase condition, we could quantitatively determine the transfer width of the instrument by means of Eq.(2-31). Also, we could quantitatively determine the average width of terraces on the surface by analysing diffuse profiles at an out-of-phase condition.

During initial experiments, we found that the symmetry of the diffraction spots and the instrumental resolution were not ideal. So, we managed to improve them further for better experimental results. We designed a round sample holder instead of a rectangular one(see figure 3.1) and modified the electron gun, as described in the next section.

3.4.3 Improvement of Instrumental Resolution and LEED Spot Symmetry

Instrumental resolution is a very important parameter which is mainly determined by the electron gun, the electrostatic lenses and the electron detector. In addition, the sample holder made of molybdenum metal might influence the focus of incident and scattered electron beams since the shape of the sample holder can affect the electric field distribution of the lens near it. From our experimental measurements, we found two problems: One was the asymmetry of the diffraction spot and the other was the resolution. In order to improve the symmetry of diffraction spots and to obtain higher resolution, we made two changes. First, we designed a round metal sample holder to replace a previous rectangular holder, since the round sample holder would not destroy the symmetry of the field of the lens nearby. The sample to be studied was put beneath the sample holder which was connected to ground. The second change involved putting an aperture with a diameter 0.7mm at the end of the electron gun to limit the electron beam diameter on the sample. The experimental results showed that the size of the electron beam on the sample reduced from about 5mm without the aperture to 2mm with it, even without using the lens in the gun. Due to the smaller size of the electron beam, the second lens(crystal lens) more easily focusses the divergent electron beam to be parallel where incident on the sample surface, and focusses diffraction electron beams well onto the

detector. With these two improvements, not only was the symmetry of diffraction spots improved but also the instrumental resolution was raised. The instrumental transfer width was increased from about 1000Å to 2000Å.

The improvement of the instrumental resolution and the diffraction spot symmetry allowed us to obtain better experimental results.

3.4.4 Effect of Channeltron Voltage on FWHM

The channeltron voltage is also an very important parameter in measuring the FWHM of spot profiles. If the channeltron voltage is set improperly, it directly influences not only the intensity but also the size of the FWHM measured. The experimental results showed that the FWHM size was basically unchanged when the channeltron voltage was controlled in the range of 2700V to 3500V. However, when the channeltron voltage was set under 2700V, the FWHM size reduced with decreasing the voltage. This is because the relationship between channeltron count rate detected and the diffracted electron beam intensity incident on it is not linear at lower voltages. As a result, to measure spot profiles and FWHM sizes correctly, we have to select a channeltron voltage in the linear region of the channeltron. Based on these results, we selected a channeltron voltage of 3100V for our experiments.

3.5 Argon Sputter Ion Gun

An argon ion gun is also an important tool for surface preparation. Here, it plays two important roles. One is to remove surface material by sputtering to clean the sample surface and the other is to produce a roughened surface by using lower controlled argon ion sputtering doses. Figure 3.9 shows a Perkin-Elmer model 2kV Sputter Ion Gun which is controlled by a model Φ20-045 Sputter Ion Gun Control. From figure 3.9, it can be seen that the gun is equipped with a focussing lens to control

the shape of the ion beam. The acceleration voltage of the ions may be controlled in the range of 0-2keV.

When we used it to sputter a sample surface, at first, the emission current was set at 25 μA and the acceleration voltage of the ions was controlled at 500V. The focus lens was set at a defocussed position. Then, we opened the control valve of argon gas and let it backfill the vacuum chamber in the range of pressure 5×10^{-6}- 5×10^{-5} Torr. The chamber of the ion gun was filled with argon gas. The electrons emitted by the hot filament were accelerated into the ionization chamber and collided with argon atoms to produce ions. The argon ions were then accelerated out of the gun onto the sample surface to be sputtered.

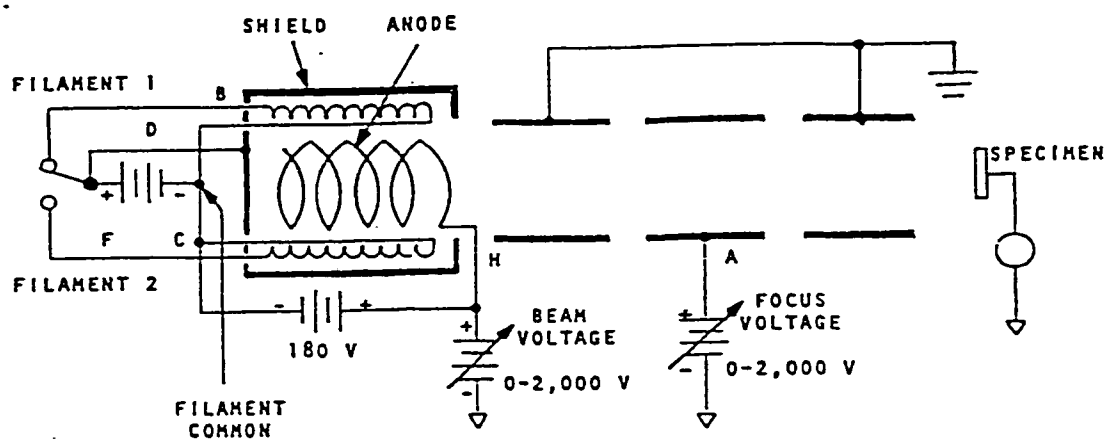

Figure 3.9 A diagram of the ion sputter gun system including the sample[3].

In order to ensure that the argon ion beam covered the whole area of the sample surface, we investigated the size of the argon ion beam on the sample surface by measuring the sample current versus a sample position which was adjusted by rotating the manipulator. We chose four different acceleration voltages. The experimental results showed that the size of the ion beam reduced with

increasing the ion acceleration voltage. When the ion acceleration voltage was set at 500V and the focus lens was set at a defocussed position, the ion beam was about 10 mm in diameter which was just consistent with the exposed size of the sample surface. This meant that the whole sample surface could be sputtered homogeneously.

3.6 Control of Annealing Temperature of Sample

In the study of surface flattening kinetics, the annealing temperature of the sample plays an important role since the annealing temperature directly influences atomic diffusion at a crystalline surface. If a change of the annealing temperature of the surface takes place during annealing, it results in a change of the atomic diffusion coefficient. As a result, we would be unable to measure the surface flattening kinetics accurately. In order to obtain more accurate results of the surface flattening kinetics, the annealing temperature must be kept constant during annealing.

The sample temperature was measured by connecting two chromel-alumel thermocouples which were glued into the grooves at the two edges of the sample. The thermocouples were monitored by a temperature controller(Eurotherm 818). The temperature controller would provide the power for the heater which was controlled to maintain the desired sample temperature steady to $\pm$ 0.1K during annealing. The control of the sample annealing temperature could be done either manually or automatically. In the manual mode, we adjusted the heater current to reach the desired annealing temperature, while in the automatic mode, the heating rate and annealing temperature were controlled by a program.

Chapter 4. Results and Analysis

In this chapter, we describe the time-resolved results of surface flattening kinetics and the effect of annealing on the terrace height distribution. Also, we describe the analysis methods and causes of errors.

4.1 Surface Morphology from the (0,0) Diffraction Spot

As seen in figure 1.3 in section 1.3, the diffraction pattern of a TiO_2 (110) surface contains many diffraction spots. From the diffraction pattern we can know the structure of the crystalline surface. Moreover, the profile of a diffraction spot contains information on the surface morphology. As a result, if we want to know information on the surface morphology we have to investigate the profile of the diffraction spot. From a theoretical point of view, for an unreconstructed (1×1) surface any diffraction spot may be chosen for the investigation of the surface morphology since it contains the same information of the surface morphology. However, in actual measurements, we chose the (0,0) diffraction spot for surface investigation for two reasons: 1) The incident electron wave vector is almost normal to the sample surface since the angle between the electron gun and the channeltron detector is small, about 7° so that the (0,0) diffraction electron beam is focussed onto the detector well and easily; 2) The energy value of an in-phase or out-of-phase condition is calculated more easily compared with that of other diffraction spots.

4.2 Determination of In-phase and Out-of-phase Conditions for the (0,0)

In several previous sections, we have mentioned the in-phase and the out-of-phase conditions but there we did not give concrete values for the TiO_2 (110) surface. In this section, we will not only

give theoretically calculated energy values but also use an experimental method to check the value of an in-phase condition which is very important for us in determining the relative weight, $G_0(k_\perp)$, of the Bragg peak since our analysis method is based on this value. If an incorrect value of the in-phase condition energy were chosen, it would result in wrong results of analysis. Therefore, we have to determine the value very carefully.

As done before in section 2.3, the momentum transfer vector from incident and scattered electron wave vectors may be split into $\mathbf{k}_\perp$ and $\mathbf{K}_{//}$. Since we analyse the (0,0) diffraction spot, we can obtain $\mathbf{K}_{//}=\mathbf{0}$ and $k_\perp = 2k_0\cos\theta \approx 2k_0$ ($\theta \approx 4^0$). In addition, from a side view (see figure 2.7) it may be seen that although the surface with steps has two different types of columns, all steps have the same height d (3.25Å). By means of Eq.(2-16), the in-phase and out-of-phase conditions of the diffraction intensity must satisfy

$$2k_0 d = n\pi, \qquad (4\text{-}1)$$

where n is an integer. If n is an even number, Eq.(4-1) shows that the scattered electron waves have the same phases(or in-phase) and add constructively in the diffraction amplitude, while, if n is an odd number, they are out-of-phase and add destructively in the diffraction amplitude. The kinetic energy of the electrons can be expressed by

$$E = \frac{\hbar^2 k_0^2}{2m}, \qquad (4\text{-}2)$$

where $\hbar$ is Planck's constant and m is the electron rest mass. If Eq.(4-1) is inserted into Eq.(4-2) and then the parameter constants are substituted into it, Eq.(4-2) can further be simplified as

$$E = 0.892 n^2 (eV). \qquad (4\text{-}3)$$

Using Eq.(4-3), we can calculate the energy values of the in-phase and out-of-phase conditions at a (110) rutile surface for the (0,0) spot. These values are partially listed in Table 4.1.

Table 4.1 Energy values of the in-phase and out-of-phase conditions.

n	10	11	12	13	14	15
E(eV)	89.2	107.9	128.5	150.7	174.8	228.3

From Table 4.1, it can be seen that the energy values of the in-phase and out-of-phase conditions alternate. In our actual measurements, we used an electron beam energy in the range of 128.5eV to 150.7eV to analyse the surface terrace height distribution. In order to determine whether the theoretically calculated values of the electron energy at the in-phase condition were correct, we carried out a verification experimentally. We collected the spot profiles at the in-phase condition and near it and plotted graphs of the spot profiles. The peak intensities were both normalized to make comparison of the profile shapes easier(see figure 4.1).

Comparing the profile shapes of figure 4.1(a), we can see that when the electron beam energy is reduced from 128.5eV to 124.5eV the diffuse shoulder begins growing up. Also, when the electron beam energy is increased from 128.5eV to 132.5eV the diffuse shoulder starts rising (see figure 4.1(b)). In addition, it is also found that when the electron beam energy is in the range of 127.5 to 129.5eV, the spot profiles almost overlap each other. As a result, the experimental result indicates that the energy value of the in-phase condition is at 128.5±1eV since the terrace height distribution at the in-phase condition does not influence its spot profile. That means the spot profile at the in-phase condition should exhibit the shape of the Bragg peak delta function and there is no diffuse shoulder profile due to the effect of the terrace height distribution. When the electron beam energy is moved away from the in-phase condition gradually, the effect of the terrace height distribution in the spot profile begins increasing so that the diffuse shoulder of the spot profile grows. From these experimental results, we have proved that the theoretically calculated value of energy at the in-phase condition is true. From this result we can further deduce that the difference of work function between the specimen surface and the filament surface does not influence the energy value at the in-phase condition significantly. Even if it does, its influence is small.

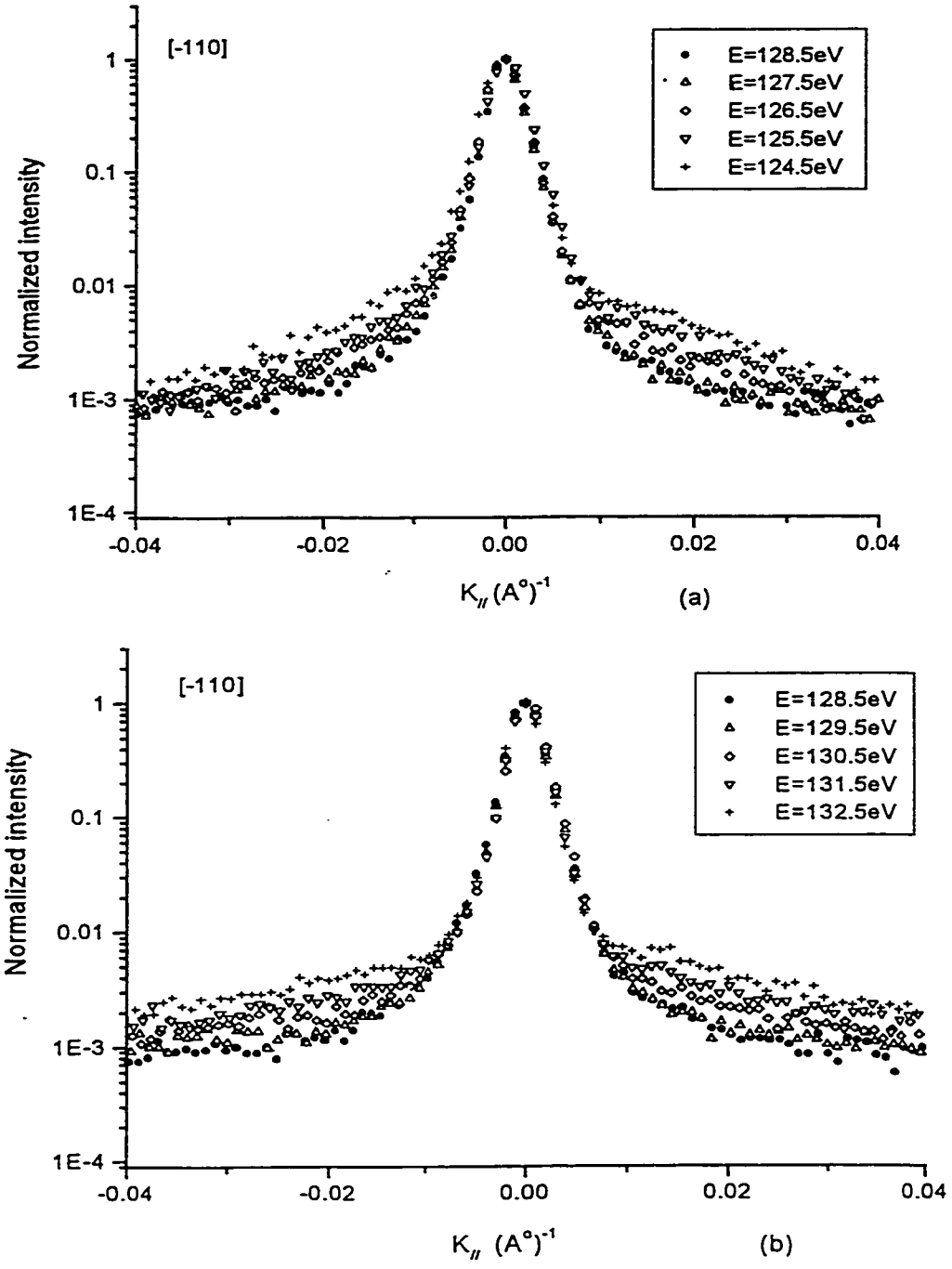

Figure 4.1 Comparison of raw data at and near the in-phase conditions. Peak intensities are normalized to 1.

4.3 Measurements of Surface Flattening Kinetics

In the introduction we reviewed the results of other researchers' measurements on surface flattening kinetics. Here, we will introduce our measurement method to determine the time-evolution of the average terrace width found by analyzing diffraction spot profiles measured during the annealing process. Before kinetics measurements, the sample surface must be roughened by bombardment with argon ions at room temperature to form a terrace height distribution which causes the diffuse shoulder of the diffraction spot profile at an out-of-phase condition. During the process of annealing the sample, the width of the diffuse shoulder will decrease due to growth of the average terrace width. By investigating the rate of reduction of the width, we can determine the time-evolution of the average terrace width from which the flattening exponent value can be determined.

4.3.1 Roughened Surface at a Low Sputtering Dose

The previous research work done by Piercy and Grossmann [1,2] was based on a higher sputtering dose (300μA·min) which produced a rougher surface since the higher sputtering dose could remove more than ten monolayers from a crystalline surface. Their experimental result showed that the flattening exponent β was close to 1/4. Here, we used a low sputtering dose and hoped to remove less than one monolayer and to produce a rough surface spanning a few levels only. On this surface, we carried out measurements to check whether the flattening exponent β was changed in comparison with the higher sputtering dose. The previous research showed that if the sputtering dose was controlled at 300μA·min and the energy of incident argon ion beam was set at 500eV, it was estimated that about 15 monolayers were removed from the crystalline surface[1]. Therefore, we chose a low sputtering dose of 10μA·min with argon ion energy 500eV.

Before the low sputtering dose, we cleaned the sample surface by using a higher sputtering dose, and then annealing the surface at 725 K for 10 minutes and then at 950 K for 20 minutes so that the

surface was clean and flat. We further used Auger electron spectroscopy to check the surface. The result showed that there were no other impurities except the tiny amount of argon ions embedded at the surface, giving an Auger peak ratio for Ar(LMM)/Ti(LMM) of about 1%. After that, the surface was sputtered by using the low dose of 10μA·min(I_{sample}=2.0±0.1μA, t=5 min) at room temperature. Note that, when we say sample current, we are including the current on the sample and its holder. After sputtering, there was a bigger defect concentration of oxygen vacancies at the surface. That is, the chemical composition at the surface of the rutile sample might be described by TiO_x with x significantly less than 2. So, the surface was immediately annealed at 725 K for 10 minutes. The speed of heating up to the annealing temperature was controlled at 2°C/s and the speed of cooling afterward was about 1°C/s in the vacuum chamber. After this short annealing, the surface returned to near-stoichiometry, that is, the value of x above approaches 2.

Before carrying out the measurements of time-resolved SPA-LEED during annealing, we checked spot profiles at the in-phase and out-of-phase conditions. Figure 4.2(a) shows their profiles from which it can be seen that the sizes of the FWHM in [-110] and [001] directions are both about 0.003

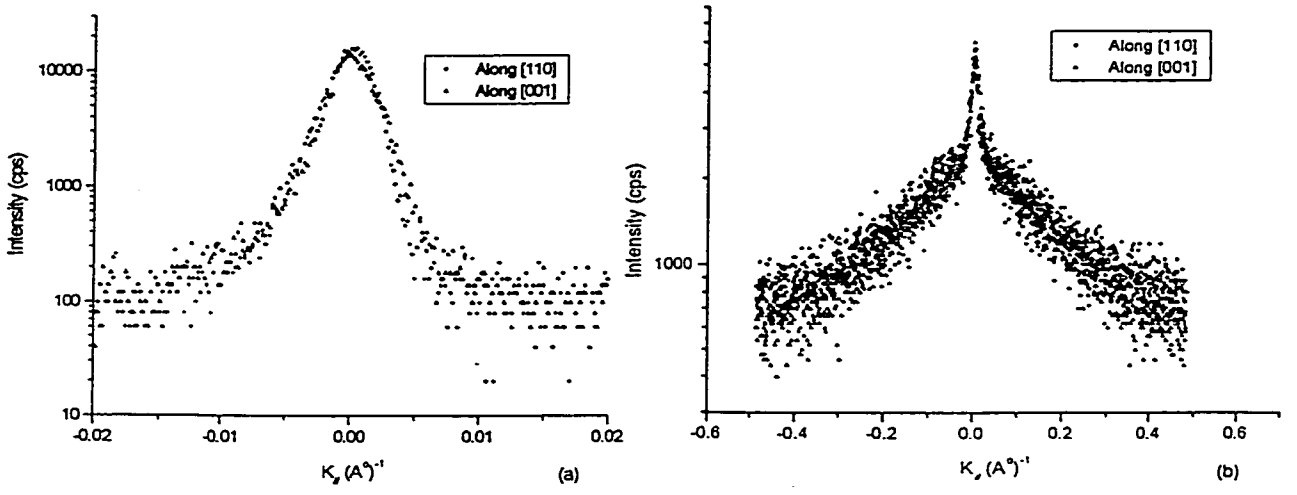

Figure 4.2 The spot profiles at the in-phase and out-of-phase conditions. Note different $K_{//}$ scale. (a) in-phase 128.5eV; (b) out-of-phase 150.5eV.

$Å^{-1}$ at the in-phase condition. In addition, we note that, at the out-of-phase condition, there was also a wider FWHM of the diffuse profile due to the effect of the terrace height distribution in the spot profile. From figure 4.2(b) it can be seen that the FWHM size of the diffuse shoulder is 0.19 to 0.24 $Å^{-1}$.

4.3.2 Time-Resolved SPA-LEED Measurements at an Out-of-Phase Condition

In the time-resolved SPA-LEED experiment, the intensity data of diffraction spot profiles along [-110] and [001] directions can be collected automatically by using commercial computer software modified by Riel, Grossmann and Piercy. The experiment may be continued for several hours while a specimen surface is being annealed. Before we carried out measurements, the sample surface was roughened as described in the previous section and then SPA-LEED instrumental parameters such as electron beam energy, filament current, and channeltron voltage were set properly. The number of raw data points recorded for every spot profile was 1000 and the scan time of every point was 50 ms. The deflection voltage was controlled in a range of 20V(the approximate Brillouin zone width). The temperature of the sample surface was controlled automatically. The sample was heated to the desired annealing temperature as quickly as possible. The average speed of heating up to the desired temperature was about $7\,^{0}C/s$. Once the surface was heated to the expected temperature of 800 K or 850 K, it was kept at this constant temperature until the end of the experiment.

After all the parameters were set up, we started to carry out the measurements of spot profiles at the out-of-phase condition and, at the same time, the measured raw data were stored into a data directory on a hard disk in a computer. The experiment generally continued for 3 hours at least.

4.3.3 Treatment of Experimental Data

After finishing the measurements mentioned above, we needed to analyze the raw data of the spot profiles since the raw data only gave us qualitative information including a Bragg peak and a diffuse

shoulder at the out-of-phase condition. However, important quantitative information could not be obtained accurately without the help of a mathematical analytical method. For example, we wanted more accurately to separate the diffuse shoulder from a spot profile and to determine the FWHM of the diffuse profile. So, we had to create a mathematical formula to fit the raw data and to obtain a best fit. From the best fitting parameters we could obtain the FWHM size and distinguish the Bragg peak delta function and diffuse shoulder in the spot profile. Our fitting procedure was based on maximizing the approximate probability function expressed by

$$P(\{y_i\},\{a_i\}) = \prod_i (\sqrt{2\pi}\sigma_i)^{-1} \exp(-\frac{\chi^2}{2}), \qquad (4\text{-}4)$$

where χ^2 is defined as

$$\chi^2 = \sum_i \frac{(y_i - y(x_i;\{a_i\}))^2}{\sigma_i^2}, \qquad (4\text{-}5)$$

where y_i is the measured experimental value, $y(x_i;\{a_i\})$ is a fitting function, and $\{a_i\}=(a_1, a_2, \ldots, a_m)$ contains m fitting parameters. σ_i is the standard deviation expressed by $(y_i/\tau)^{1/2}$ (τ: gate time). If the χ^2 value reaches a minimum, the probability function $P(\{a_i\})$ reaches a maximum. This means that the parameters $\{a_i\}$ have maximum probability. So we call the parameters of the maximum probability the best parameters. Based on the shape of the spot profile at the out-of-phase condition, we adopted a Gaussian function for the Bragg peak broadened by the instrumental response and a Lorentzian function for the diffuse shoulder caused by the terrace height distribution as the mathematical formula which was expressed by

$$y(x_i;\{a_i\}) = a_1 e^{-a_2(x-a_5)^2} + \frac{a_3}{(1+a_4(x-a_5)^2)^{a_7}} + a_6, \qquad (4\text{-}6)$$

where a_6 is the background intensity. a_1 and a_3 are the amplitudes of the Bragg peak and diffuse shoulder, respectively. a_5 is the center position of the peak of the spot profile. a_4 is used to determine the HWHM value. The values of a_2 and a_7 were fixed and the rest of the parameters were fitted. The value of a_2 was determined from the full width at half maximum of the Bragg peak delta function and a_7 was given by $a_7=(1+d)/2$, where the value of d is the dimension of the Lorentzian function chosen for fitting the diffuse profiles. For d=1, $a_7=1$ and the fitting function has the form of a one-dimensional Lorentian function. For d=2, $a_7=1.5$ and the fitting function has the form of a two-dimensional Lorentian function.

4.3.4 Analysis of Results

From the experimental measurements and fitting results above, we got qualitative knowledge. The average terrace width increases with annealing time. In order to get the fundamental quantitative power law of surface flattening kinetics, we plotted a log-log graph of the average terrace width, l(t)=2/HWHM, versus annealing time in figure 4.3. From the figure it can be found that the average terrace width l(t) increases by roughly 3 times over the time interval from 1 to 100 minutes.

From the analysis results of figure 4.3, it can be seen that the average terrace widths in the two different directions varying with annealing time at 800 K were fitted by a power law $l(t)\propto t^{\beta}$. The fitting results show that the β values of the power law for [-110] and [001] directions are 0.25 and 0.22, respectively. If we chose to fit over annealing times from 20 min to 140 min, the β values for [-110] and [001] are both 0.25. These results were obtained by using a one-dimensional Lorentzian function ($a_7=1$). If we used a two-dimensional Lorentzian function ($a_7=1.5$) to fit the diffuse profiles, the values of the flattening exponent β for [-110] and [001] are 0.24 and 0.20, respectively. Compared with the results using the one dimensional Lorentzian function, the values of the flattening exponent are slightly smaller, but the difference is not large.

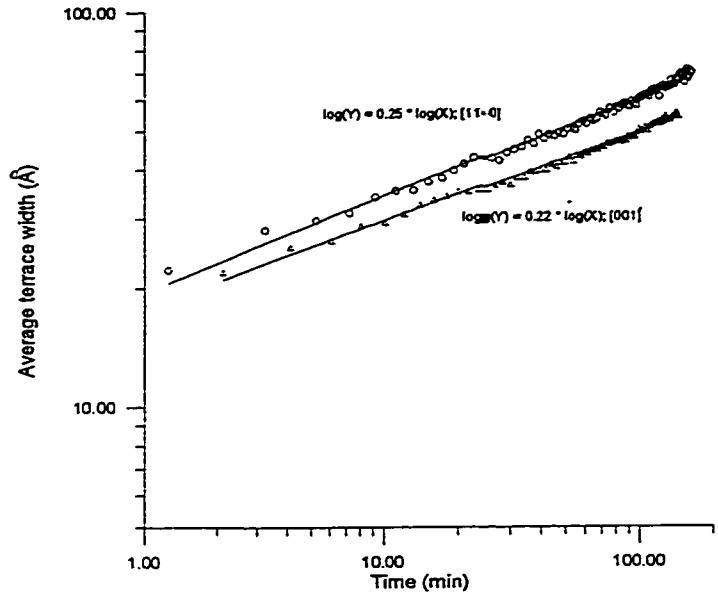

Figure 4.3 The average terrace width varies with annealing time at 800 K.

Using the same method, we analysed data at the higher annealing temperature of 850 K. From the analysed results of figure 4.4, it can be seen that, for a one-dimensional Lorentzian function, the β values of power law for [-110] and [001] are both 0.24. If we observe figure 4.4 carefully, we can see

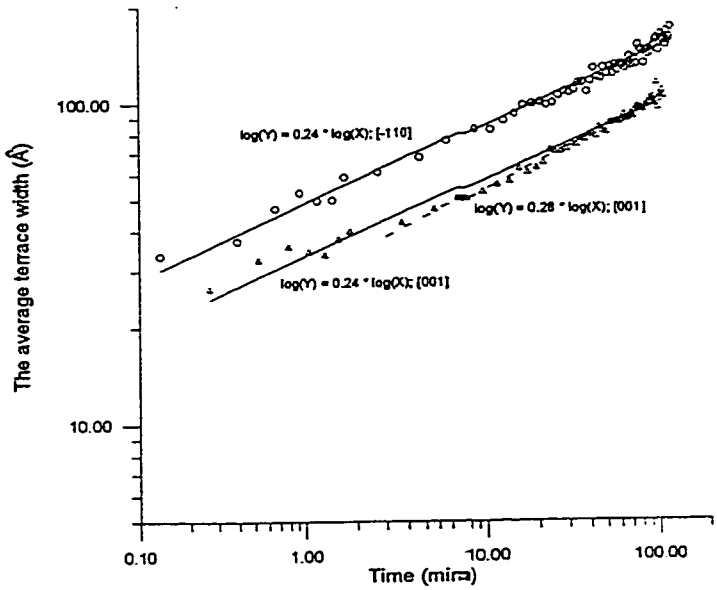

Figure 4.4 The average terrace width varies with annealing time at 850 K.

that the fitting result for [001] direction is not very good since there are more points lower than the fitted line. At early time, the average terrace width versus annealing time might be a curve. If we chose the time range from 3 to 130 minutes. the value of the flattening exponent β was 0.28 (dashed line). If we used a two-dimensional Lorentzian function instead, the β values of power law for [-110] and [001] were changed to 0.23 and 0.21, respectively.

From the above results, it can be seen that the measured values of exponent β for the growth of the average terrace width (l(t)) differ by ≤ 0.04, comparing data in different crystallographic directions or at different annealing temperatures. In addition, we estimate that a systematic error in β of about 15% could be introduced by the choice of fixed parameters a_2 and a_7 and the fitted data range. In summary, we obtain an average measurement of the flattening exponent $\beta=0.24\pm0.04$.

4.3.5 Comparison of High and Low Sputtering Doses

The results given above are similar to that of previous experiments after the higher sputtering dose done by Piercy and Grossmann [1,2]. Their flattening exponent β fell in the range 0.23-0.25 at annealing temperatures of 800 and 850 K. The experimental result after the low sputtering dose tells us that even though the surface has a flatter initial condition, the measured flattening exponent β basically does not change. In order to understand the similar flattening exponents after the higher and low sputtering doses, we investigated the effect of annealing on the terrace height distribution in the next section.

4.4 Determination of the Terrace Height Distribution and Interface Width

In this section, we focus on discussing the effect of annealing on the terrace height distribution and the interface width after the surface is sputtered by argon ions at the low or higher sputtering dose. In order to do so, we had to do SPA-LEED experiments to record spot profiles for a range of electron beam energies from the in-phase condition to the out-of-phase condition at room temperature after

different annealing times at 800K. Similar to the treatment in section 4.3.3, we built a mathematical formula to fit the shape of a spot profile and to distinguish the Bragg peak and the diffuse shoulder. Based on the results of the best fit, the relative weight $G_0(k_\perp)$ of the Bragg peak versus electron beam energy (or phase) was calculated by using a numerical integration and then plotted as a graph from which we could determine the terrace height distribution and calculate the interface width.

4.4.1 Methods of Determining the Terrace Height Distribution and Interface Width

In section 2.3 we introduced the definition of the interface width in terms of Eq.(2-25). In this section we will show how to determine the interface width and the terrace height distribution. So far, there are three methods to determine interface widths, using 1) the data near the in-phase condition, 2) the half width of the relative weight curve $G_0(k_\perp)$, and 3) the terrace height distribution. No matter which way we determine the surface interface width, at first we must determine the relative weight $G_0(k_\perp)$ varying with electron beam energy by means of Eq. (2-23). We will briefly introduce the three methods as follows:

1) Near the in-phase condition[1,22]

Let us assume that the perpendicular momentum transfer $k_\perp$ is close to the in-phase condition. The electron wave phase, $dk_\perp$, may approximately be expressed by

$$dk_\perp = 2\pi l + d\delta k_\perp, \qquad (4\text{-}7)$$

where l is an integer and $d\delta k_\perp \ll 2\pi$ near an in-phase condition. Before we expand the exponential within the brackets in Eq.(2-19) we define the moments $M_v(\mathbf{l})=d^v\langle(h(\mathbf{m}+\mathbf{l})-h(\mathbf{m}))^v\rangle$. We insert Eq. (4-7) into Eq.(2-19) and expand with respect to $d\delta k_\perp$. The structure factor can be expressed by[22]

$$G(\frac{2l\pi}{d}+\delta k_\perp, \vec{K}_{//}) = \sum_l (\sum_v \frac{1}{v!} M_v(\vec{l})(-id\delta k_\perp)^v e^{-\vec{K}_{//}\cdot\vec{r}_l} \quad . \qquad (4\text{-}8)$$

For odd ν all the moments vanish. As a result we only consider even moments $M_{2\nu}(l)$. Since $d\delta k_\perp$ is a very small amount, we keep the lowest moment term $M_2(l)$ and all the higher terms are neglected. Eq.(4-8) may be further rewritten as

$$G(\frac{2\pi l}{d}+\delta k_\perp, \vec{K}_{//}) = (1-w^2(\delta k_\perp)^2)G_{ideal}(\vec{K}_{//}) + w^2(\delta k_\perp)^2\Omega(\vec{K}_{//}) \quad . \qquad (4\text{-}9)$$

Comparing Eq.(4-9) with Eq.(2-21) we find that the relative weight $G_0(k_\perp)$of the Bragg peak may be expressed by[22]

$$G_0(k_\perp) \approx 1 - w^2(\delta k_\perp)^2 \qquad (4\text{-}10)$$

By using Eq.(4-10), we can plot a graph of $G_0(k_\perp)$ versus $(\delta k_\perp)^2$ in the vicinity of the in-phase condition and determine the interface width from the slope of the $G_0(k_\perp)$ curves. Although this method is simpler to determine the interface width by calculating several points of $G_0(k_\perp)$ which are close to the in-phase condition, it cannot provide the full terrace height distribution.

2) **Half width of relative weight curves $G_0(k_\perp)$**

In this method, $G_0(k_\perp)$ values from the in-phase condition to the out-of-phase condition need to be calculated. From the $G_0(k_\perp)$ curve we can measure the half width at half maximum of $G_0(k_\perp)$ (see figure 4.5). Then, we use the Gaussian approximation to determine the interface width which is expressed by

$$w = \frac{d\sqrt{\ln 2}}{\delta\phi_{1/2}}, \qquad (4\text{-}11)$$

where w is the interface width and $\delta\phi_{1/2}$ is the half width. d is the height of steps at the surface. Like method 1) near the in-phase condition, this method cannot provide the terrace height distribution at the surface. However, the method is more convenient to analyse interface widths qualitatively

according to Eq.(4-11). For example, when the half width of a $G_0(k_\perp)$ curve increases, the corresponding interface width is reduced and the surface becomes flatter. Otherwise, the surface becomes rougher.

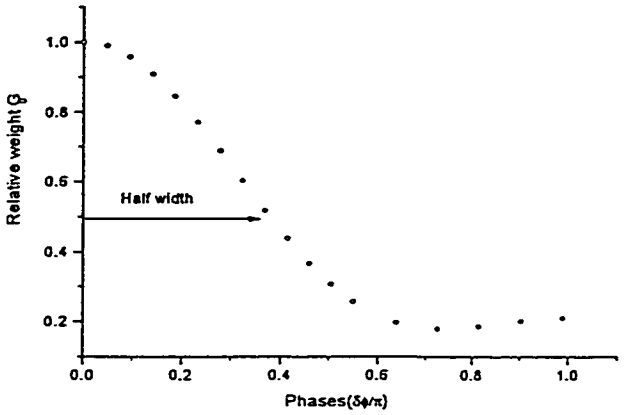

Figure 4.5 The relative weight, $G_0(k_\perp)$, of the Bragg peak varies with phase.

3) Terrace height distribution

Similar to the previous method, to obtain the terrace height distribution we also need to determine $G_0(k_\perp)$ values from the in-phase condition to the out-of-phase condition. However, the difference is that this method uses Eq.(2-22) to fit the relative weight curve $G_0(k_\perp)$. From the fitting results we can obtain the terrace height distribution. In order to fit the $G_0(k_\perp)$ curves easily, Eq.(2-22) may be further rewritten as

$$G_0(k_\perp) = \left| 1 - \sum_{n=1}^{N} \theta_n + \sum_{n=1}^{N} \theta_n e^{in\phi} \right|^2 , \qquad (4\text{-}12)$$

where θ_n is the exposed coverage of the n^{th} level and $\phi = k_\perp d$. We use Eq.(4-12) to fit the relative weight curve $G_0(k_\perp)$ to get the best parameters $\{\theta_n\}$. Based on these parameters $\{\theta_n\}$ and the definition of the interface width in Eq.(2-25), we can further deduce the interface width as follows

$$w^2 = \sum_{n=1}^{N} n^2 \theta_n - (\sum_{n=1}^{N} n\theta_n)^2 . \qquad (4\text{-}13)$$

Using Eq.(4-13), we can work out the interface width based on the terrace height distribution. As a result, we preferred to use this method to analyse the surface since it can not only determine the interface width but also provide the information of the terrace height distribution.

4.4.2 Determination of $G_0(k_\perp)$ after Low or High Sputtering Doses

From the above discussion, we know that, no matter which method we choose, we must at first determine $G_0(k_\perp)$ values from experiments. According to Eq.(2-23), we have to determine the ratio of the integrated Bragg peak intensity to the total integrated intensity. In order to get these integrated intensities, we need to analyse every spot profile and to separate the Bragg peak from the spot profile by using a mathematical formula. We carried out SPA-LEED experimental measurements of after both low and higher sputtering doses.

For the low sputtering dose, the experimental procedure was similar to that of measuring the flattening exponent β. At first, the sample surface was cleaned by argon ion sputtering at the dose of 200 μA*min followed with annealing at 725 K for 10 minutes and at 950 K for 20 minutes which made the surface nearly stoichiometric and flat. After the sample was cooled to room temperature in the vacuum chamber, the sample surface was sputtered at the low dose of 10 μA*min and then annealed at 725K for 10 min. Following that, the surface was annealed at 800 K for different annealing times. After each annealing stage, we carried out the SPA-LEED measurements from the in-phase condition to the out-of-phase condition at room temperature. The annealing time at 800 K is listed in Table 4.2.

Table 4.2 Annealing times at 800 K after the low sputtering dose.

Temp.(K)	725	800	800	800	800	800	800
Time (min)	10	0.2	0.8	4	5	20	70
Cumulative annealing time(min) at 800 K	0	0.2	1	5	10	30	100

During measurements, we selected the electron beam energy in the range of 123.5eV-156.5eV which covered from the in-phase to the out-of-phase condition. In the range of 123.5eV-140.5eV, we recorded the spot profiles varying with the electron beam energy in steps of 1eV, while, for the rest energies, they were collected in steps of 2eV.

For the higher sputtering dose, the experimental procedure was similar to that of the low sputtering dose except using a 200 μA*min instead of 10 μA*min dose. In addition, there was a little difference in annealing time which is shown in Table 4.3. From the SPA-LEED measurements, we found that after the low sputtering dose and then annealing at 725 K for 10 min, the (0,0) diffraction spot at the out-of-phase condition could be observed while, after the higher sputtering dose and annealing at 725 K for 10 min, the (0,0) diffraction spot at the out-of-phase condition could not be found. This fact shows that the crystalline surface after the higher sputtering dose is rougher than that produced by the low sputtering dose.

Table 4.3 Annealing times at 800 K after the higher sputtering dose.

Temp.(K)	725	800	800	800	800	800
Time (min)	10	1	5	4	20	70
Cumulative annealing time(min) at 800 K	0	1	6	10	30	100

4.4.3 Analysis of Diffuse Shoulder Profiles at the In-phase Condition

In section 2.4, we discussed the instrumental response and resolution. We know that, for a rough

stepped surface without other defects such as impurities and point defects, the distribution of diffraction intensity at the in-phase condition only depends on the instrumental response rather than the surface response. That is, an ideal spot profile at the in-phase condition looks like the Bragg peak broadened by the instrumental response, while there should be no diffuse shoulder. However, in our actual measurements, we found that each of the measured spot profiles at the in-phase condition contained a diffuse shoulder besides the Bragg peak(see figure 4.6). From figure 4.6 it can be seen that the FWHM sizes of the Bragg peak and diffuse shoulder are 0.003-0.004 $Å^{-1}$ and 0.11-0.14 $Å^{-1}$, respectively. In addition, the analysed results showed that the integrated intensity of the diffuse profile was no less than that of the Bragg peak at the in-phase condition. This made our analysis more complicated than for ideal spot profiles. At other electron beam energies, the terrace height distribution of the surface also causes a diffuse profile. This means that, for non-ideal spot profiles, except at the in-phase condition, the diffuse profile consists of the effects of both the terrace height distribution and other defects. So, we couldn't directly extract the effect of the terrace height distribution in the spot profile like for an ideal spot profile. In order to separate the effect of the terrace height distribution from the diffuse profiles correctly, we had to analyse what caused the diffuse shoulder at the in-phase condition.

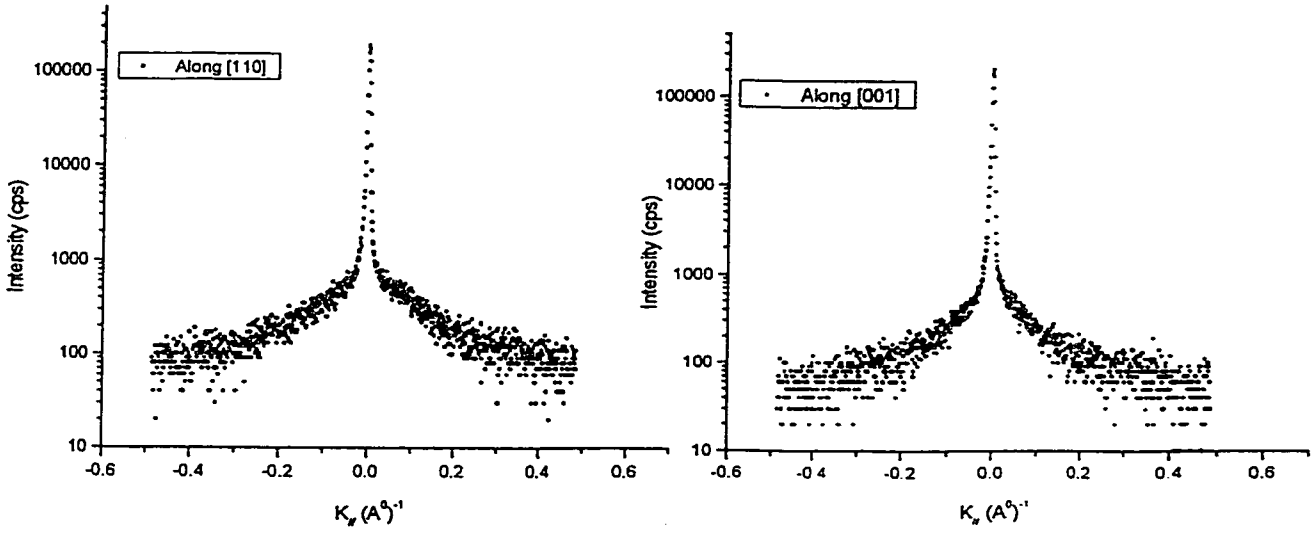

Figure 4.6 Spot profiles in [-110] and [001] directions at the in-phase condition.

We did a lot of different experiments to investigate what causes the diffuse shoulder at the in-phase condition. For example, we carried out experiments of the effect of annealing time on diffuse profiles at the in-phase condition (see figure 4.7). From figure 4.7, it can be seen that the diffuse

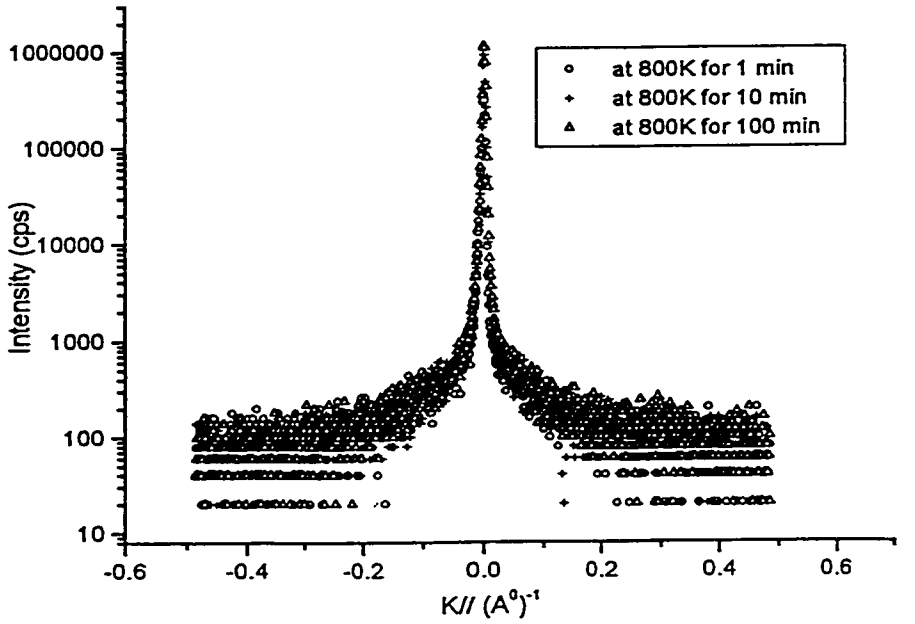

Figure 4.7 The surface was annealed at 800 K for 1, 10, 100 min.

shoulders have no obvious change with increasing annealing time from 1 min to 100 min. If the diffuse shoulder results from point defects at the surface, after a long period of annealing time, the density of the point defects might be expected to be reduced. A change of the density of the point defects will affect the diffuse shoulder. However, the experimental result shows that the diffuse shoulder has no obvious change. The experimental result suggests that the diffuse shoulder at the in-phase condition does not come from point defects at the surface. According to the results of different experiments, we think that the diffuse shoulder at the in-phase condition might come from our instrument itself. As a result, we could consider the whole spot profile (Bragg peak plus diffuse shoulder) at the in-phase condition as a convolution of the Bragg peak delta function with the instrumental response function which is expressed by

$$y = y_o + Ae^{\frac{(x-x_c)^2}{2\sigma^2}} + \frac{B}{(1+\frac{(x-x_c)^2}{w^2})^{1.5}} + \frac{C}{(1+\frac{(x-x_c)^2}{d^2})^{1.5}} \quad , \qquad (4\text{-}14)$$

where A, B, and C are the amplitudes of the Bragg peak, narrow shoulder and diffuse shoulder,

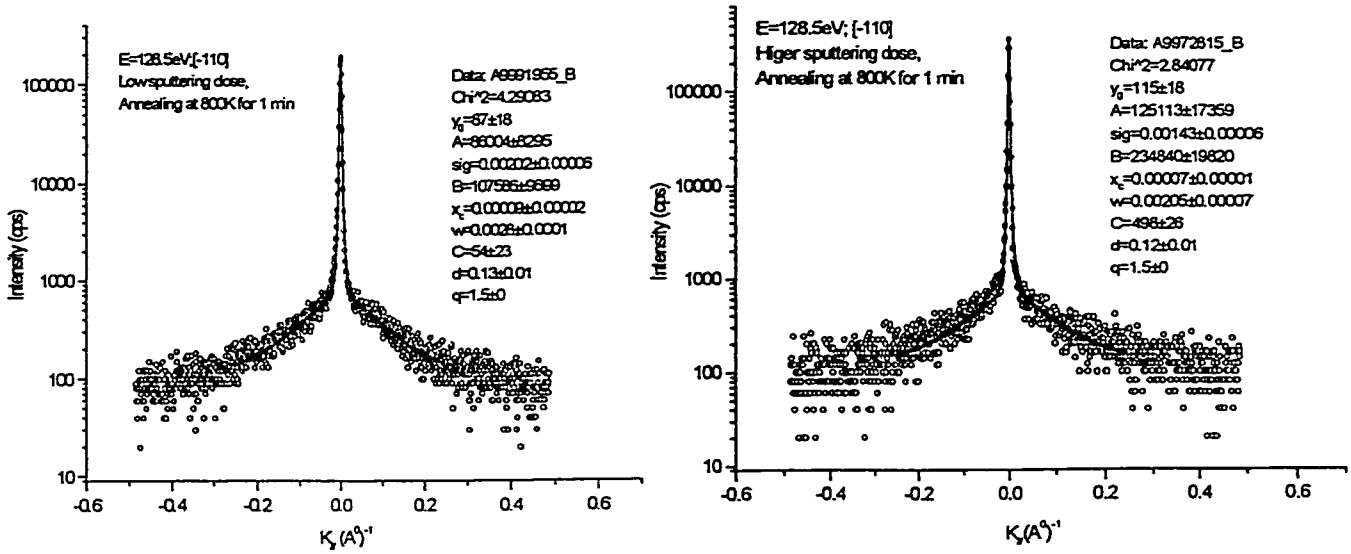

Figure 4.8 The fitted results at the in-phase condition.

respectively. σ is the width of the Gaussian and w and d are the half widths of a narrow and diffuse shoulder. We used Eq.(4-14) to fit the spot profiles at the in-phase condition. The fitted results are shown in figure 4.8.

4.4.4 Mathematical Formula for Non-ideal Profiles

In the previous section, we put forward the whole spot profile at the in-phase condition as the instrumental response function, based on our experimental analysis. As a result, like that of an ideal spot profile, a mathematical formula for a non-ideal profile at an arbitrary phase condition may also be expressed by

$$y = y_o + Dg(x,\sigma) + \frac{S}{(1+\frac{(x-x_c)^2}{t^2})^q}, \qquad (4\text{-}15)$$

where y_o is the background intensity. D is the amplitude of the delta function and S is the amplitude of the diffuse shoulder caused by the terrace height distribution. t is the half width of the diffuse profiles. g(x, σ) is the instrumental response function expressed by

$$g(x,\sigma) = he^{-\frac{(x-x_c)^2}{2\sigma^2}} + \frac{h_1}{(1+\frac{(x-x_c)^2}{(r_1\sigma)^2})^{1.5}} + \frac{h_2}{(1+\frac{(x-x_c)^2}{(r_2\sigma)^2})^{1.5}}. \qquad (4\text{-}16)$$

The function g(x, σ) of the instrumental response is based on the fitting result of Eq.(4-14) (see figure 4.8). Where h=A/(A+B), h_1=B/(A+B), h_2=C/(A+B), r_1=w/σ, and r_2=d/σ. The ratios h, h_1, h_2, r_1 and r_2 are considered to be approximately constant, and independent of electron beam energy.

Using Eq.(4-15) we fitted the spot profiles from the out-of-phase condition to near the in-phase condition. The fitted results at the out-of-phase condition are shown in figure 4.9. From fitted results

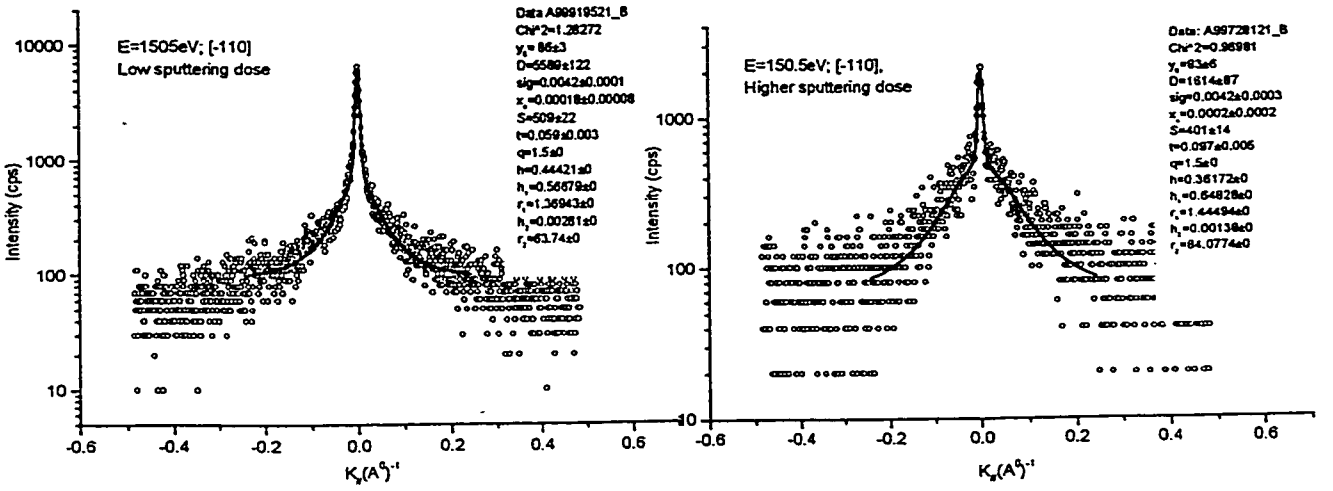

Figure 4.9 The fitted results at the out-of-phase condition.

we could determine the FWHM sizes which are 0.09Å^{-1} for the low sputtering dose and 0.15Å^{-1} for the higher sputtering dose after annealing for 1 min. The analysed result also indicates that the surface is rougher after the higher sputtering dose than after the low sputtering dose.

In addition, for the spot profiles in the vicinity of the in-phase condition (129.5-132.5 eV), we found that Eq.(4-15) could not be fitted very reliably. In order to solve this problem we spent a lot of time to build different mathematical formulas to analyse the profiles. We tried to test many different fitting methods such as fitting raw data of both crystallographic directions at the same time and reducing the range of $\mathbf{K}_{//}$ included in the fit, based on Eq.(4-15). We found that, although the problem still existed, including a narrower $K_{//}$ range in the fit gave better results. The main difficulty is that, when the electron beam energy is close to the in-phase condition, the effect of the terrace height distribution in the diffuse profile is so small that it is difficult to distinguish its effect in the spot profile more accurately.

4.4.5 Numerical Integration of Diffraction Intensity

Based on the parameters of the best fit using Eq.(4-15), we may calculate the intensity of the Bragg peak and the diffuse profile using analytical or numerical integration methods. However, due to the asymmetry of spot profiles, the values of fitting parameters such as D or S are different in [-1 1 0] and [0 0 1] directions so that analytical integration cannot be used very well. As a result, we had to use numerical integration instead.

4.4.6 Error Calculation of G_0 Values

Before giving the results we need briefly to discuss the error calculation of the relative weight $G_0(k_\perp)$. According to the definition of statistical error, the error of the relative weight $G_0(k_\perp)$ may be expressed by

$$\Delta G_0 = (\sum_{i=1}^{m} (\frac{\partial G_0(\{\vec{a}_i\})}{\partial a_i})^2 (\Delta a_i)^2)^{\frac{1}{2}} \quad . \qquad (4\text{-}17)$$

Eq.(4-17) is suitable for the analytical integration method. However, although it also works for the numerical integral method, we use another formula for the error instead of Eq.(4-17) in order to save time. The formula is expressed by

$$\Delta G_0 = (\sum_{i=1}^{m} (G_0(\{a_i^0 i \neq j\}, a_j^0 + \sigma_j) - G_0(\{a_i^0\}))^2)^{\frac{1}{2}}, \qquad (4\text{-}18)$$

where $\{a^0_i\}$ is the best fit result based on Eq.(4-15) and σ_i is the standard deviation of the parameter a^0_i. Based on Eq.(4-18), the error of the relative weight $G_0(k\perp)$ can be calculated. Here, we need to mention that we use the software of Origin version 5.0 to fit the measured spot profiles using the Levenberg-Marquart method.

4.4.7 Analysis of Results

Before giving analysis of results, we compared the sizes of the HWHM at the out-of-phase condition measured by both time-resolved SPA-LEED during annealing and SPA-LEED at room temperature between annealing stages. The fitted HWHM results are shown in figure 4.10.

From figure 4.10, it can be clearly seen that the size of the HWHM measured by SPA-LEED at room temperature is slightly lower than that done by time-resolved SPA-LEED during annealing. The difference might come from the effect of temperature on the spot profiles or the influence of history of the sample treatment shown in section 4.5.2. If we use a power law to fit the HWHM values from SPA-LEED at room temperature, the slope of the HWHM is about 0.22-0.24 which is similar to the exponent value found previously in section 4.3.4. This figure illustrates that the two experiments have

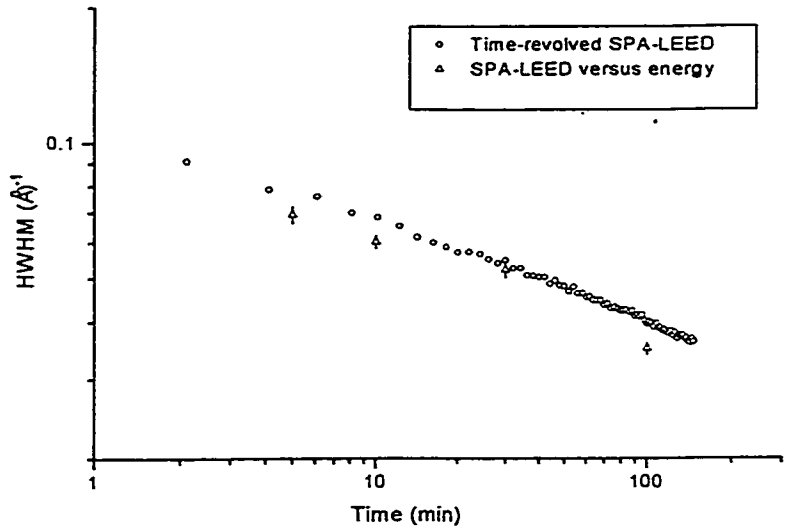

Figure 4.10 HWHM vary with increasing annealing time at 800 K after the low sputtering dose.

similar results at the out-of-phase condition. That is, we may investigate the effect of annealing on the terrace height distribution by collecting spot profiles at room temperature after different annealing times.

Now we study the relative weight $G_0(k\perp)$ versus electron beam energy at different annealing times shown in figure 4.11. From figure 4.11(a) corresponding to the low sputtering dose it can be found that the relative weight $G_0(k\perp)$ increases with annealing time at a fixed phase. The increase of the $G_0(k\perp)$ value indicates that the crystalline surface is flattening. For the higher sputtering dose(see figure 4.11(b)), at or near the out-phase condition, the relative weight $G_0(k\perp)$ increases with annealing time. However, when the phase approaches the in-phase condition, the $G_0(k\perp)$ values after annealing time for 1 min or 100 min do not obey the above rule but the rest of the values obey the rule. We use the half width of the $G_0(k\perp)$ curve to estimate the interface width. For the low dose case, it can be found that the half width at $G_0(k\perp)=0.5$ varies from 0.41π to 0.47π. According to Eq.(4-11), the calculated interface width falls in the range 1.8 Å - 2.1 Å. The change of interface width is estimated

to be about 0.3 Å. For the higher dose case, the half width of $G_0(k_\perp)$ at 0.5 varies from 0.25π to 0.32π which corresponds to the interface width in the range 2.8 Å - 3.5Å. The change of the interface width is about 0.7 Å.

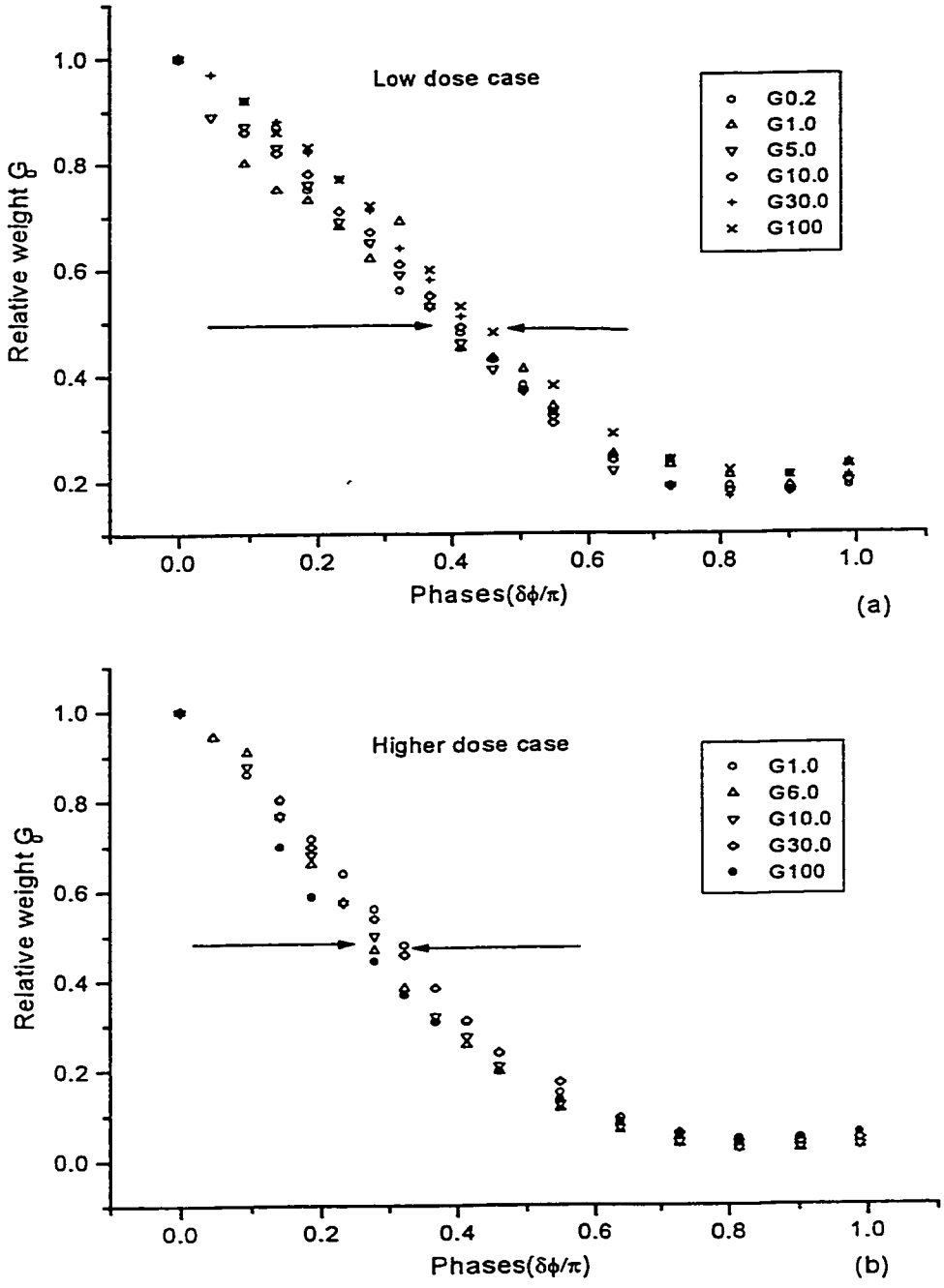

Figure 4.11 The relative weight $G_0(k_\perp)$ varies with phases at different annealing times.

We quantitatively determine the terrace height distribution by fitting the relative weight $G_0(k_\perp)$ versus phase after different annealing times. The statistical error of the relative weight $G_0(k_\perp)$ was calculated by using Eq.(4-18). The calculated results show that the relative statistical errors of $G_0(k_\perp)$ fell in the range of 3-5%. So, we selected a maximum 5% as the relative statistical error of the relative weight $G_0(k_\perp)$. During fitting, we used this statistical error as weighting. Based on Eq.(4-12), we selected a five-level system to fit the relative weight curve $G_0(k_\perp)$ for the low and higher dose cases. For the low sputtering dose, the fitting results after different annealing times from 0.2 min to 100 min at 800 K are shown in figure 4.12 in which we can see the fitted curves and fitting results. Based on the fitting results we can obtain the coverage θ_n, of every terrace level listed in Table 4.4. From Table 4.4 it can be seen that the coverage of each level is different and that with increasing annealing time the coverage of each level almost stays constant although it has a small fluctuation. The total coverage of the first three levels is at least 97% of the total surface; the coverages of θ_3 and θ_4 are so small that they may be neglected.

Table 4.4 The coverage varies with increasing annealing time after the low sputtering dose.

Coverage Annealing time (min)	θ_0 (%)	θ_1 (%)	θ_2 (%)	θ_3 (%)	θ_4 (%)
0.2	63 ±1	25.6 ±0.5	8.0 ±0.5	1.6 ±0.5	1.7 ±0.5
1	64 ±2	25.2 ±0.8	8.1 ±0.8	1.8 ±0.8	1.1 ±0.9
5	61 ±1	27.0 ±0.5	8.9 ±0.5	0.7 ±0.5	2.0 ±0.5
10	62 ±1	27.6 ±0.5	8.4 ±0.5	0.4 ±0.5	1.7 ±0.5
30	62 ±1	28.2 ±0.3	8.4 ±0.3	0.0 ±0.3	1.4 ±0.3
100	66 ±1	26.1±0.3	6.6 ±0.3	0.2 ±0.3	1.3 ±0.3

For the higher sputtering dose, the fitting results after the different annealing times from 1 min to 100 min are shown in the figure 4.13. Based on the fitting results the coverage of every level is

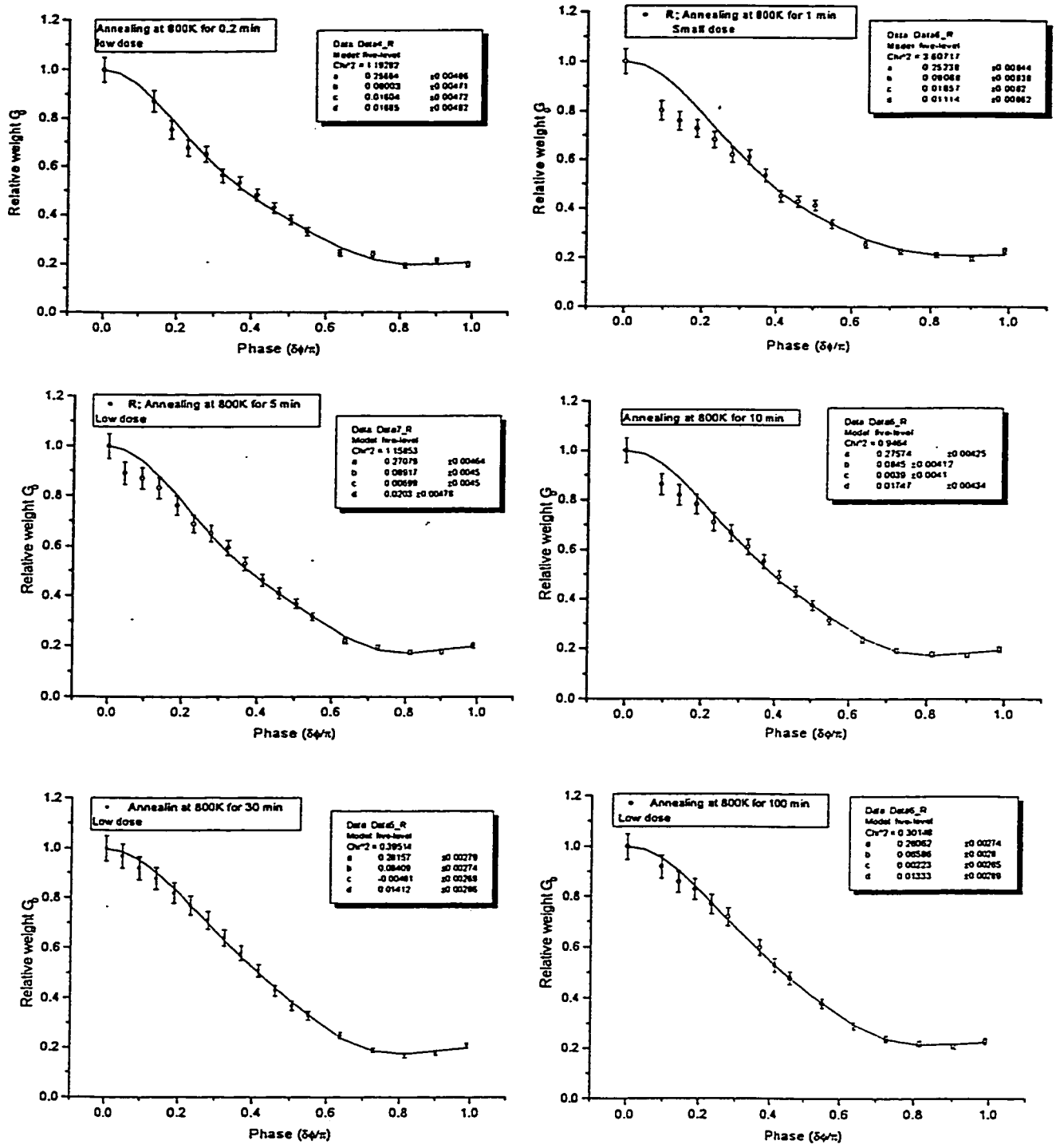

Figure 4.12 The terrace height distribution at the surface varies with different annealing times at 800 K after the low sputtering dose.

obtained and listed in Table 4.5. From Table 4.5, it is found that the coverage of every terrace level stays relatively constant although there are small fluctuations. The total coverage of the first three levels occupies about 93% of the total surface.

Table 4.5 The coverages vary with increasing annealing time after the higher sputtering dose.

Occurrence Annealing time (min)	θ_0 (%)	θ_1 (%)	θ_2 (%)	θ_3 (%)	θ_4 (%)
1	43 ±1	36.7 ±0.3	16.6 ±0.3	2.8 ±0.3	1.4 ±0.3
6	38 ±1	36.4 ±0.3	17.7 ±0.3	5.0 ±0.3	2.6 ±0.3
10	39 ±1	36.5 ±0.3	17.1 ±0.3	4.5 ±0.3	2.5 ±0.3
30	44 ±1	36.1 ±0.3	15.0 ±0.3	3.2 ±0.3	2.0 ±0.4
100	42 ±1	32.4±0.6	16.0 ±0.5	5.6 ±0.6	3.5 ±0.6

Now we compare the terrace height distribution after the low sputtering dose with that after the higher dose(see figure 4.14). From figure 4.14, it can clearly be seen that the coverage of the first level in the low dose case is about 20% larger than that in the higher dose case while the coverages of the other levels in the low dose case are smaller than those of the higher dose case. In addition, for both cases, more than 93% surface atoms occupy one of the first three levels.

In addition, from figures 4.12 and 4.13, we can see that in the range of phase $\delta\phi$=0.4 (136.5eV) to 1.0(150.5eV), the fitting curve and the data $G_0(k_\perp)$ with error bars match very well. However, when approaching the in-phase condition, the fitting curve and the data $G_0(k_\perp)$ with error bars do not fit very well. This might come from systematic errors while in figures 4.12 and 4.13, the indicated error bars are statistical errors. Fortunately, the bigger systematic errors near the in-phase condition do not influence our fitting results. Whether we remove these data near the in-phase condition or keep them, the fitting results of the terrace height distribution basically stay the same, within the range of statistical errors. Therefore, we can say that the analysed results above may be accepted.

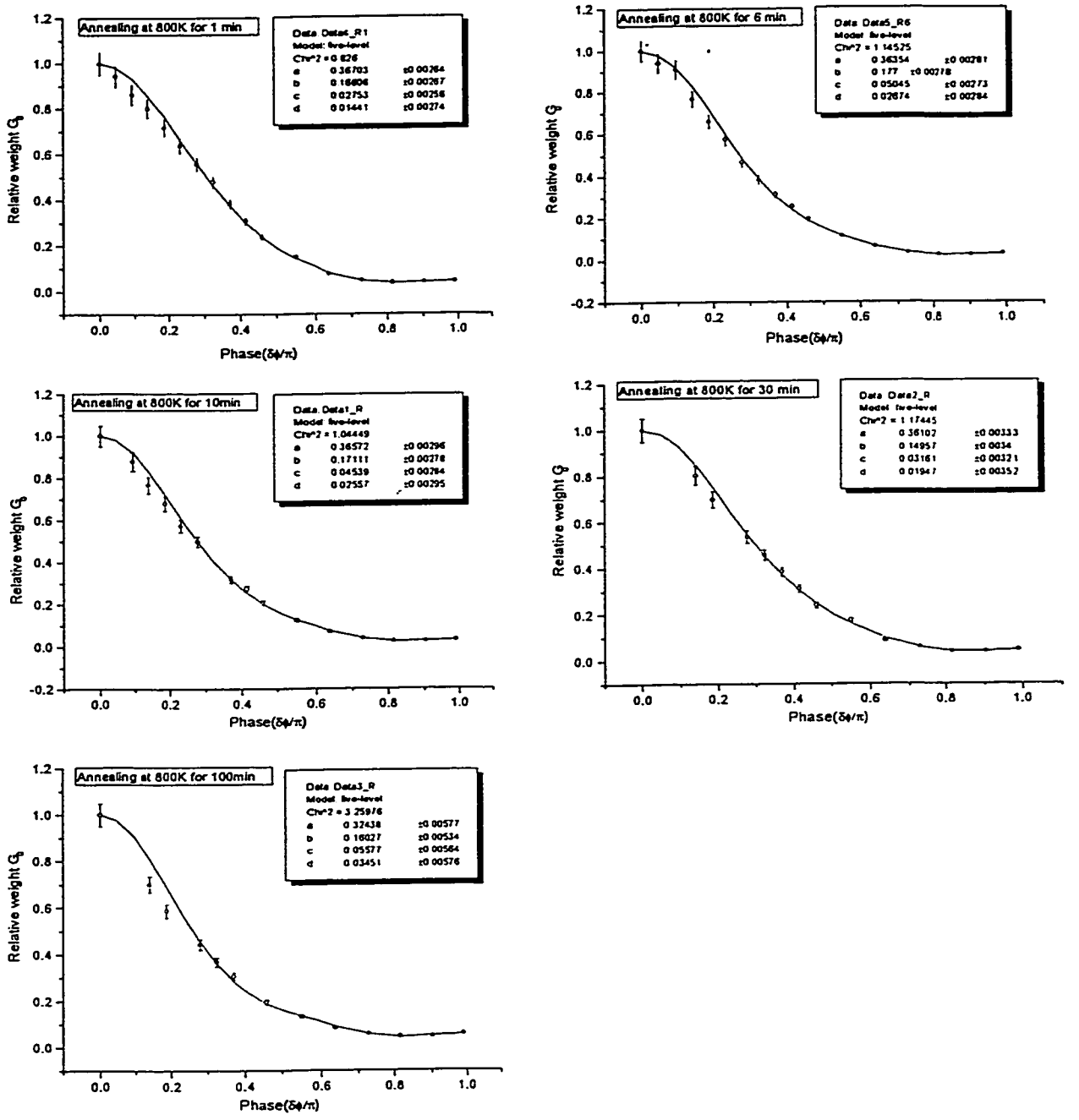

Figure 4.13 The terrace height distribution at the surface varies with different annealing times at 800 K after the higher sputtering dose.

Using the terrace height distributions of Table 4.4 and Table 4.5, we can further determine the interface width versus annealing time from Eq.(4-13). The calculated results are shown in figure 4.15 from which it can be clearly seen that the interface width after the low sputtering dose is smaller than that after the higher sputtering dose. With increasing annealing time at 800 K the interface width after the low sputtering dose reduces slightly while that after the higher sputtering dose increases slightly. Note that the average terrace width increased from 20Å to 60-70Å at 800 K for 100min. In addition, comparing the result of the terrace height distribution with that of method (2) using the half width of the $G_0(k\perp)$ curve, we can see that for the low dose case, the interface widths from the two methods are consistent. They have similar values, within error bars, and the same tendency to decrease with annealing time. For the higher dose case, the interface widths from the two methods have similar values. The method using the terrace height distribution shows that the interface width increases slightly while the method using the half width of the $G_0(k\perp)$ curve predicts that the interface width reduces slightly. This difference could come from systematic errors. Considering the error bars, we may say that the interface widths stay roughly constant at about 2.2Å for the low dose case and at about 3.0Å for the higher dose case.

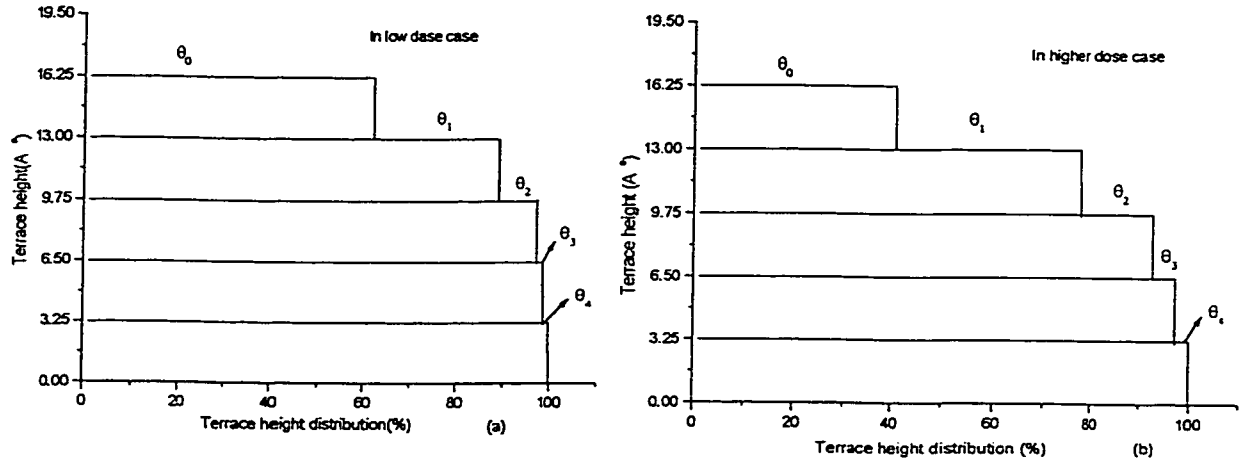

Figure 4.14 The terrace height distribution after the low or higher sputtering dose.

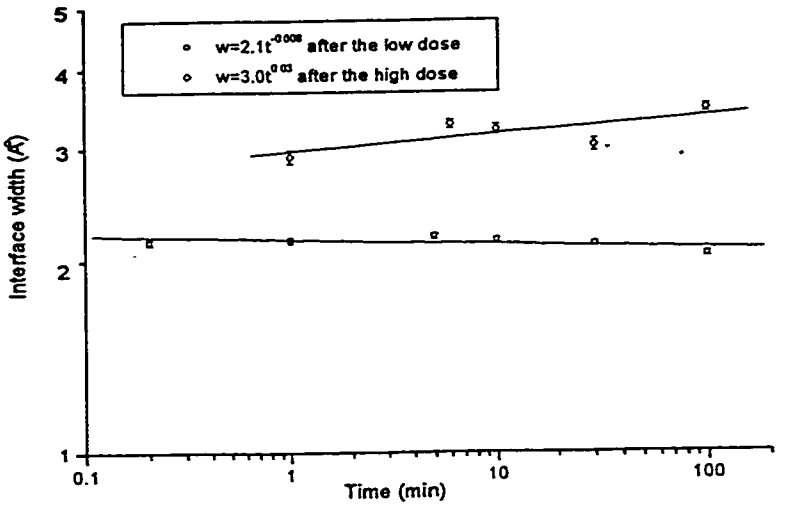

Figure 4.15 The interface width varies with annealing time.

4.4.8 Verification of Terrace Height Distribution

In the previous section, we did not mention that when we fitted the relative weight $G_0(k_\perp)$ versus phase by using Eq.(4-12), we found that there were two possible solutions for the terrace height distribution: In one solution θ_0 is at the top and θ_4 is at the bottom as shown in figure 4.14 and the other is the reverse. In reality, we expect that only one of these solutions is correct. For the higher sputtering dose, we cannot determine which one is correct after many layers have been removed. However, for the low sputtering dose, we can determine which one is possible. In order to determine which one corresponds to our actual terrace height distribution after the low sputtering dose, we carried out a still lower dose experiment (5μA*min). From the results of the SPA-LEED measurements, we found that, at the out-of-phase condition, the spot profile after a 5μA*min sputtering dose is similar to that before the sputtering except for the difference in the Bragg peak height. The result tells us that only a small fraction of a monolayer at the surface was removed. The few small islands and vacancies formed will give a broad spot profile that is too weak to be distinguished from the background. In this case, we may assume that the surface after the 5μA*min

sputtering dose is a two-level system.

For a flat surface, the diffraction intensity may be deduced from Eq.(2-18) to be $I=cN^2$ when N approaches a very large number, where c is the form factor and N is the total number of unit cell columns at the surface and assumed to be large. After the 5μA*min sputtering dose, we assume that N_2 unit cells are removed from the surface and N_1 unit cells still stay at the surface. Below the removed unit cells, there are N_2 unit cells exposed in the layer below. At the out-of-phase condition, we can obtain the formulas for the diffraction intensities before and after sputtering

$$I_b = c_0 N^2, \qquad I_a = c_0 (N_1 - N_2)^2, \tag{4-19}$$

where I_a and I_b are the intensities of the Bragg peak after and before the surface is sputtered and partially annealed, respectively. c_0 is the constant at the out-of-phase condition. In order to determine the number N_2 of unit cells removed, Eq.(4-19) can be rewritten as

$$\frac{N_2}{N} = \frac{1}{2}\left(1 \mp \sqrt{\frac{I_a}{I_b}}\right). \tag{4-20}$$

Based on the spot profiles measured by SPA-LEED, we carried out fitting and then calculated the diffraction intensity of the Bragg peak by using the numerical integration. The calculated results are listed in Table 4.6.

From Table 4.6, it can be seen that, in the lowest sputtering dose, the number of the removed unit cells at the surface is about 0.22 monolayer(ML) and that, after the 10μA*min sputtering dose, the number of the removed unit cells is between 0.47 and 0.54ML. These rough results are consistent with the relationship of $\theta_{5\mu A*min}=\theta_{10\mu A*min}/2$, expected where the sputter yield is proportional to incident ion dose.

Table 4.6 The diffraction intensity of the Bragg peak.

Condition	Dose(μA*min)	Intensity	N_2/N
flat surface	0	8511	-
lowest sputtering	5	2155	0.22
low sputtering	10	41	0.47- 0.54

In addition, according to the terrace height distribution, we may calculate the number of unit cells removed from the surface by using the following formula

$$\Theta = \sum_{n=1}^{n} n\theta_n , \qquad (4\text{-}21)$$

where Θ is the number of the removed unit cells. Based on the data of Table 4.4, we calculate that about 0.5 ML of unit cells is removed from the surface by the 10μA*min sputtering dose. This result is consistent with the relationship between the sputter yield and the incident ion dose. If the distribution were upside-down, about 1.5ML would have to have been removed. This result disagrees with the relationship of sputter yield proportional to the incident ion dose. As a result, we confirm terrace height distribution shown in figure 4.14 after the low sputtering dose.

From the above analysis result, we are sure that about 0.5ML could be removed from a TiO_2 (110) surface after a 10μA*min sputtering dose with Argon ions at 500eV and annealing at 725K for 10 minutes in vacuum.

4.5 Causes of Experimental Errors

From the experimental results above we find that our experiments were successful and our analysis methods and final results are reasonable. Even so, the accuracy of our experiments was limited by factors such as our instrument and our sample surface. We will analyse these factors.

4.5.1 Instrumental Causes of Errors

In section 4.4.3, we analysed the diffuse shoulder of the spot profiles at the in-phase condition and showed that the diffuse shoulder might come from our instrument itself. Due to this diffuse profile at the in-phase condition, we had to create a more complicated mathematical formula and used it to fit other spot profiles. In Eq.(4-15), we suppose that the form of the instrumental response function $g(x,\sigma)$, determined at the in-phase condition, is unchanged at other electron energies. However, during experiments, we found that the form of the instrumental response function at the in-phase condition changed slightly with the sample current. This results in changes of the ratios of the amplitudes and widths in Eq.(4-16) (see figure 4.16). Even though changes in the ratio h_2 are very small, its influence will be bigger for fitting spot profiles near the in-phase condition since the amplitude, D, of the delta function is large.

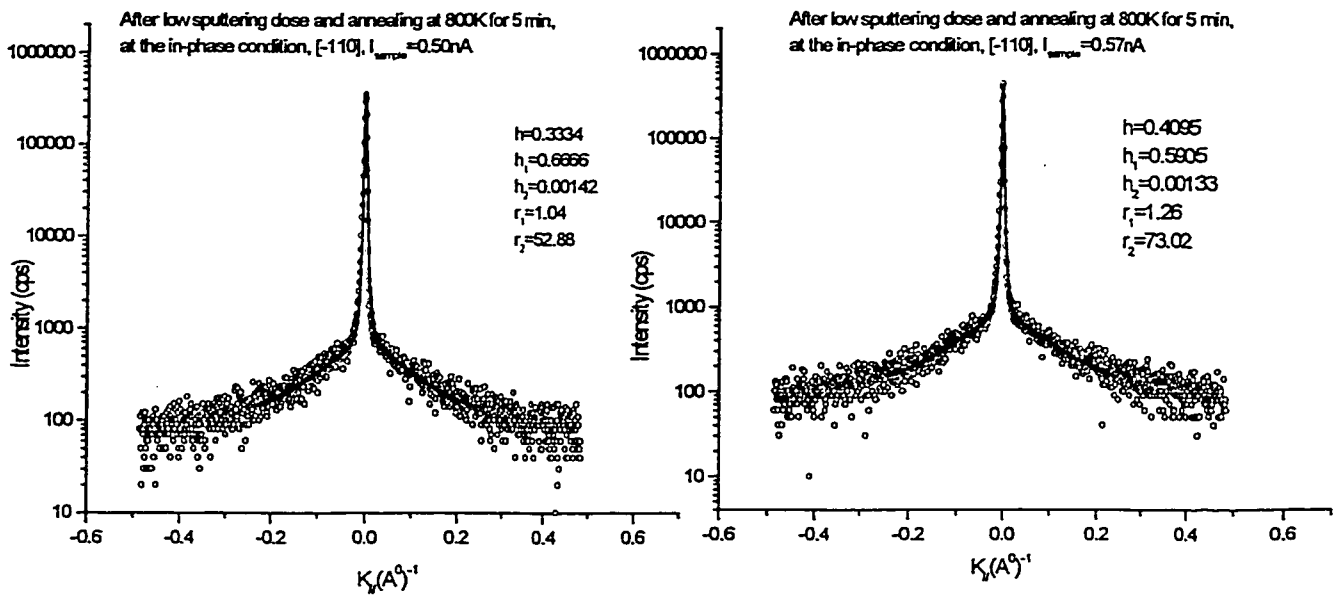

Figure 4.16. The spot profiles of the in-phase condition at different sample currents.

From figures 4.12 and 4.13, it can be seen that some $G_0(k_\perp)$ points near the in-phase condition deviate from the fitted curves. The deviation near the in-phase condition could be due to a slight

change in shape of the instrumental response function with the sample current and with energy, combined with the fact that the effect of the terrace height distribution in the spot profile near the in-phase condition is too small to be distinguished more accurately.

4.5.2 Sample Surface Treatment

Other defects at the sample surface also influence the measurements. From the history of our sample treatment we found that the spot profiles changed with sample treatment history. From figure 4.17, it can be seen that after the same sputtering dose and annealing temperature as well as time, the spot profiles at the out-of-phase condition depend on sample treatment history. In the earlier life of the sample, the spot profiles showed smaller intensities of the Bragg peak delta function. However, in later life, after many treatments of sputtering and annealing, the intensities of the Bragg peak delta function increased by about 5 times, and at the same time, the FWHM of the diffuse profile reduced slightly. This is why we see the slight difference of the HWHM sizes in figure 4.10.

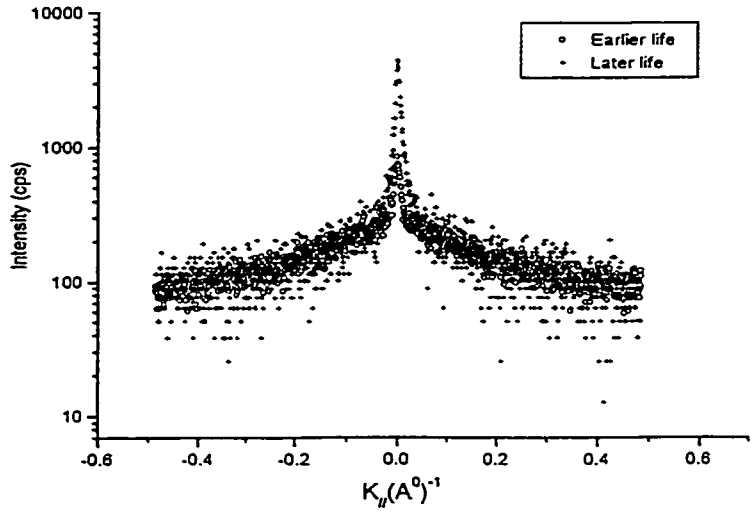

Figure 4.17 The spot profiles at the out-of-phase condition change with sample treatment history.

From our experimental conditions, the relative error in the low sputtering dose was 5%. That is

10.0±0.5μA*min. The relative error of annealing temperature is about 2%. We think that these experimental uncertainties do not cause the change of the Bragg peak intensity in spot profiles mentioned above. The change of the Bragg peak intensity might result from point defects at the sample surface. We do not think that the point defects come from impurities since the amount of the impurities is very small, about 1% according to AES experimental results.

Chapter 5. Discussion

In this chapter we will mainly discuss our experimental results and compare them with other researcher's results. We also discuss our analysis methods.

5.1 Comparison of Average Terrace Widths from STM and SPA-LEED

As mentioned in the introduction, there are two main methods to investigate surface morphology and defects: One is diffraction techniques and the other is imaging techniques. In 1994, Onishi and Iwasawa[23]used STM to investigate reconstruction of a TiO_2 (110) surface. From their published STM image after the TiO_2 (110)(1×1) surface was sputtered and then annealed at 860K for 30 seconds, we estimate that the average terrace widths on the surface in [-110] and [001] directions are about 90Å and 50Å, respectively. These results are obtained by us, using the intercepting line method to analyse their STM image shown in figure 5.1. From our experimental results shown in figure 4.4, it can be found that after the TiO_2 (110)(1×1) surface was sputtered at a low dose and then annealed at 850K for 30 seconds the average terrace widths in [-110] and [001] directions are about 40Å and 28Å, respectively.

Comparing the two experimental results, we find that the average terrace widths measured by the STM image are about twice as big as those determined by the SPA-LEED method. The difference might come from several reasons: 1) The two crystalline surfaces might have different initial roughened conditions and different average terrace widths. From Onishi and Iwasawa's experimental description, it can be found that their sample surface was sputtered by argon ions with acceleration voltage 3kV for 5 minutes.(They did not provide the sample current.) Our sample surface was

bombarded by argon ions with acceleration voltage 0.5kV for 5 min and the sample current(including the holder current) was controlled at 2.0±0.1μA. From their STM image, it can be found that after sputtering and annealing at 800 K, the crystalline surface shows a seven-level system at least, while our analysed results show that our crystalline surface contains approximately three levels after the low sputtering dose and then annealing at 800K. Note that these results follow ion bombardment with different acceleration voltages. Argon ions of different energies have different penetration depths at a TiO_2 (110) surface. As a result, the different energies of argon ions produced different initial surfaces. 2) The STM image and the SPA-LEED method have different analysed field areas. The STM image shows a smaller surface area of about 35×35 nm^2 while the SPA-LEED measurement covers a surface area of about 4 mm^2. The STM field of view contains a few terraces or islands so that it can not represent the average properties of the whole surface morphology while the results of the SPA-LEED measurement better represent the surface morphology since the SPA-LEED measurement covers a much bigger area than the STM image. Therefore, we can say that the average terrace widths determined by SPA-LEED method are more accurate than those measured from an STM image.

Figure 5.1 STM image taken by Onishi and Iwasawa[23].

Although the average terrace widths measured from the STM image are different from those determined by the SPA-LEED method, they have the same order of magnitude. Therefore, the result of the STM image can support our experimental results qualitatively.

5.2 Flattening Exponent β

The studies of surface flattening kinetics now mainly focus on determining the surface flattening exponent β. In order to determine its value, a lot of experimental studies have been done by many researchers for different materials. There are two methods to produce an initial rough surface spanning only a few levels: One is to use MBE to deposit a few monlayers on a substrate and the other is to use argon ion sputtering to remove atoms from a substrate. Then, using the SPA-LEED technique, one measures the surface flattening exponent. So far there have been some experimental results which show that the flattening exponent β varies mainly between 1/5 and 1/3. These measured results come from different single crystal materials such as Cu, Si, and TiO_2.

In the introduction, we reviewed the theories of surface flattening kinetics. Among them, the classical continuum model put forward by Mullins[6] was based on three assumptions: (i) the initial surface z=W(x,y,t=0) lies everywhere near the reference plane z=0 and has no steep slopes; (ii) all surface properties of the solid are independent of crystallographic orientation; (iii) the solid is restricted to one component for all transport mechanisms except viscous flow. For surface diffusion only, and assuming an initial height distribution at the surface corresponding to a delta function "hill" at the origin (W(x,0,t=0)=αδ(x) or W(x, y, t=0)=αδ(x)δ(y)), with the help of mathematical tools, Mullins derived the following formula of surface flattening kinetics

$$d = C_0 (Bt)^{\frac{1}{4}}, \qquad (5\text{-}1)$$

where d is the lateral correlation length which is from x=0 to the first minimum of the Green's function, C_0=4.6 corresponds to one-dimensional diffusion and C_0=5.0 for two-dimensional diffusion.

$B=D_s\gamma\Omega\upsilon/kT$, where D_s is the surface diffusion coefficient, γ is the surface energy per unit area, Ω is the atomic volume, and υ is the number of molecules per unit area of surface. From Eq.(5-1), it can be seen that the correlation lateral length d follows a power law with exponent $\beta=1/4$. From our experimental results, it can be seen that the value of the flattening exponent β equals 0.24 ± 0.04 which is close to 1/4. Although the value is consistent with the predicted result of Mullins' theory, the surface flattening mechanism is different from Mullins's surface flattening mechanism since we study the discreet average terrace width while Mullins studied the continuum lateral correlation length. Moreover, during annealing, the average terrace width at our sample surface increases but the interface width stays nearly constant within error bars. However, Mullins' flattening theory tells us that the lateral correlation length at the surface is increasing and, at the same time, the interface width is reducing.

In addition, as described in the introduction, Mullins's theory is only applied above the roughening transition temperature, T_R, above which the surface exhibits a round microscopic morphology so that there are no cusps of surface tension. However, below T_R, there is a cusp of surface tension at the surface so that this results in the failure of Mullins' theory. Due to this problem, Rettori and Villain developed the theory of a bidirectional sinusoidal modulation at a crystalline surface. They thought that kink atoms at the surface mainly diffuse from ledges of small islands to those of large islands and deduced the following chemical potential of an atom on a ledge of average island radius R_n

$$\mu_n = G_3\left(\frac{1}{l^3{}_n} - \frac{1}{l^3{}_{n+1}}\right) + \frac{g}{R_n}, \qquad (5\text{-}2)$$

where μ_n is defined as the free energy loss per atom when an atom moves from a ledge of one island to others. G_3 is a constant from a Taylor expansion for the free energy, G, per unit projected surface area. l_n is equal to R_n-R_{n-1}. Based on Eq.(5-2), below T_R, they further derived that the height is a linear

function of time t and that the lifetime τ is proportional to $h(0)\lambda^3$.

From their theoretical result, it may be seen that, if h(0) is proportional to λ, $\tau \propto \lambda^4$. This result suggests that, below T_R, the value of surface flattening exponent in this case may be 1/4. For a random surface which lies everywhere near the reference z=0, Mullins' integral solution[7] gives $d \propto t^{1/4}$. Although the exponent value of Rettori and Villain's theory is similar to that of our flattening exponent measured below T_R, their flattening mechanism also is different. So far, the theories of surface flattening kinetics predict a reduction in the interface widths with increasing annealing time. However, our results show that the average terrace width increases with annealing time while the interface width stays nearly constant within error bars.

5.3 Terrace Height Distribution at Surfaces

Now, let us consider a Poisson distribution of depths at a surface. The formula of the Poisson distribution is expressed by

$$P_n = \frac{1}{n!} l^n e^{-l}, \qquad (5\text{-}3)$$

where P_n is the coverage of the n^{th} level at a surface and l indicates the average number of monolayers removed from the surface. According to Eq.(5-3), we can calculate the Poisson distribution of depths at a surface as shown in Table 5.1, for different average sputter depths l.

For the low sputtering dose, we compare Table 4.5 with Table 5.1. It can be found that the measured terrace height distribution is very close to that of a Poisson distribution for l=0.40 or 0.50. The result is consistent with that of our analysis in section 4.4.8. However, for the higher sputtering dose (200μA*min), about ten monolayers might be removed from the surface. The measured terrace height distribution in Table 4.6 is different from that of a Poisson distribution in this case. It appears that the Poisson distribution is only suitable for the low dose case here.

Table 5.1 Poisson distribution of depths at a surface.

l(ML)	θ_0(%)	θ_1(%)	θ_2(%)	θ_3(%)	θ_4(%)	θ_5(%)	θ_6(%)
0.25	78	19	2	0.2			
0.40	67	27	5	0.7			
0.50	61	30	8	1	0.2		
0.75	47	35	13	3	0.6		
1.00	37	37	18	6	2		
2.00	14	27	27	18	9	4	1
5.00	0.67	3.5	8.4	14	17	17	14
10.00	4.5×10^{-3}	4.5×10^{-2}	0.23	0.8	1.9	3.7	9.0

The calculated result of theory by using a Poisson distribution supports our experimental analysis result of the terrace height distribution for the low sputtering dose.

5.4 Interface width

Based on the terrace height distribution, we obtain the interface width using Eq.(4-13) versus annealing time shown in figure 4.15. From figure 4.15, it can be seen that the interface width after the low sputtering dose is smaller than that after the higher sputtering dose. With increasing annealing time, for the low dose case, the interface width reduces slightly while for the higher dose case the interface width increases slightly in comparison with the increase of the average terrace width. Therefore, we can say that the interface widths after the low or higher sputtering dose are about 2.2Å and 3.0Å within error bars, respectively.

In previous work done by Piercy and Grossmann[1], the interface width determined by using the data near the in-phase condition was 2.7Å after a higher sputtering dose(300μA*min) and then annealing at a temperature of 800K for 20 min. At the same conditions of the annealing temperature and annealing time but different sputtering doses(we used the sputtering dose of 200μA*min), the interface width determined by using the method of the terrace height distribution is about 3.0Å. From

the two results, it can be seen that there is no big difference in the interface widths between the two analysis methods. The small difference might come from the different sputtering doses and systematic errors.

From Yang, Wang and Lu's work[36], their experimental results show that the interface width reduces slightly with increasing annealing time. In addition, Wollschlager and Henzler's experimental results[22] show that annealing cannot drastically improve the quality of the interface width at a surface which spans a few levels. Their experimental results basically are consistent with ours. As a result, from our experimental results and others, we can conclude that with increasing annealing time, the interface width in a few-level system stays nearly constant within error bars or changes very slowly.

Chapter 6. Conclusion

From SPA-LEED studies on a roughened TiO_2 (110)(1×1) crystalline surface, we determined not only a surface flattening exponent by analysing time-resolved spot profiles at the out-of-phase condition but also the terrace height distribution and interface width versus annealing time after the low or higher sputtering dose by measuring and analysing spot profiles varying with electron energy from the in-phase condition to the out-of-phase condition. The concrete conclusions are summarized as follows:

1) The exponent value β ($I(t) \propto t^{\beta}$) of surface flattening kinetics at the TiO_2 (110)(1×1) surface below a roughening transition temperature, T_R, equals 0.24±0.04, close to 1/4, even for a surface with the smaller interface width of about 2.2Å. Although the flattening exponent value is consistent with the result of Mullins' theory, the flattening mechanism at the surface spanning only a few levels is different from Mullins's theory as well as other theories of surface flattening kinetics.

2) The average terrace width increases with annealing time. During annealing from 1 to 100 minutes, the average terrace width increases by roughly three times. The average terrace width determined by SPA-LEED is the same order of magnitude as that of the STM image.

3) The terrace height distribution and interface width stay nearly constant within error bars with increasing annealing time at 800K after the low or higher sputtering dose. For the low dose case, the total coverage of the first three levels is at least 97% of the total surface and the interface width is about 2.2Å. For the higher dose case, the total coverage of the first three levels occupies 93% of the total surface and the interface width is about 3.0Å.

4) About 0.5ML is removed from the TiO_2 (110) surface after the low sputtering dose (10μA*min) with 500eV argon ions and annealing at 725K for 10 min. In this case, we determine the terrace

height distribution shown in figure 4.14(a). However, for the higher sputtering dose, there are two possibilities of the terrace height distribution: One is shown in figure 4.14(b) and the other is upside-down. For this case we cannot determine which one corresponds to the real surface as for the low dose case but we think that the terrace height distribution shown in figure 4.14(b) is the most probable one.

5) For the low sputtering dose, the terrace height distribution at the surface is consistent with a Poisson distribution of depths. From this discussion, we conclude that the Poisson distribution is only suitable for the low sputtering dose case.

6) From the experimental results above, we can deduce that, at this few-level system, the diffusion of atoms from the ledges of smaller terraces to that of bigger ones takes place only on the same level but the probability of atoms jumping from one level to others is very small. This might come from the effect of the potential barriers at steps on diffusing atoms.

Appendix

Appendix 1:

For a stepped TiO_2(110) surface, there are two different column types which are shown in figure A1. The different columns result in different dynamic scattering factors. As a result, we have to consider this difference. According to Eq.(2-11), the diffraction intensity is expressed by

$$S(\vec{k}_0,\vec{k}_s)=\sum_m\sum_n f_n(\vec{p})f_m^*(\vec{p})e^{i\vec{k}\cdot(\vec{\rho}_n-\vec{\rho}_m)}. \qquad \text{(A1-1)}$$

For an a-type column, the scattering factor, $f_n(\mathbf{p},a)$, may be written as

$$f_n(\vec{p},a)=\int_{-a/2}^{a/2} f_a(x)e^{iK_{//x}x}dx=\int_0^{a/2} f_a(x)(e^{iK_{//x}x}+e^{-iK_{//x}x})dx, \qquad \text{(A1-2)}$$

where $f_a(x)=f_a(-x)$ because of tetragonal symmetry and a indicates magnitude of primitive lattice vector($\mathbf{a}_1$). $f_a(x)$ is denoted as

$$f_a(x)=\int_{-c/2}^{c/2}dy\int_{-\infty}^{0}dz\sum_i f_i(x,y,z)\delta(\vec{r}-\vec{r}_i), \qquad \text{(A1-3)}$$

where an atom i at $\mathbf{r}_i$ is in an a-type column. Also, for a b-type column, the scattering factor, $f_n(\mathbf{p},b)$, may be indicated as

$$f_n(\vec{p},b)=\int_{-a/2}^{a/2} f_b(x)e^{iK_{//x}x}dx=\int_0^{a/2} f_b(x)(e^{iK_{//x}x}+e^{-iK_{//x}x})dx. \qquad \text{(A1-4)}$$

From the geometrical shape of a and b type columns, we can see that $f_b(x)=f_a(x-a/2)$. As a result, Eq.(A1-4) may further be rewritten as

$$f_n(\vec{p},b) = e^{iK_{//}a/2} f_n(\vec{p},a) + \int_0^{a/2} f_a(x) e^{iK_{//x}x} (e^{iK_{//x}a/2} - e^{-iK_{//x}a/2}) dx. \qquad \text{(A1-5)}$$

Because the second term on the right side is small, it may be ignored. As a result, Eq.(A1-5) may be further rewritten as

$$f_n(\vec{p},b) \cong e^{iK_{//x}a/2} f_n(\vec{p},a). \qquad \text{(A1-6)}$$

Based on Eq.(A1-6), for a stepped TiO_2 (110)(1×1) surface, the diffraction intensity may further be expressed by

$$S(\vec{k}_0, \vec{k}_s) = |f_n(\vec{p},a)|^2 \sum_m \sum_n e^{i\vec{k}\cdot(\vec{\rho}_n - \vec{\rho}_m)} e^{iK_{//x}(s_n - s_m)a/4}, \qquad \text{(A1-7)}$$

where if the column is a-type, s_n=1, and if the column is b-type, s_n= -1.

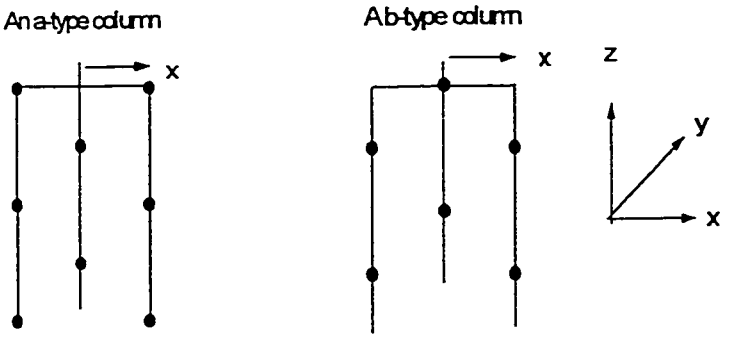

Figure A1 Two different types of columns at a TiO_2 (110) surface.

Appendix 2:

The structure factor G(**k**) can be split into two terms, one is G_δ of the Bragg peak delta function and the other is G_{diff} of the diffuse profile caused by the terrace height distribution. G(**k**) is expressed by

$$G(\vec{k}) = G_{\delta}(\vec{k}) + G_{diff}(\vec{k}). \qquad \text{(A2-1)}$$

In addition, $G_{\delta}(\mathbf{k})=G_0(k_{\perp})G_{ideal}(K_{//})$, where $G_0(k_{\perp})$ is the relative weight of the Bragg peak which varies with $k_{\perp}$ and $G_{ideal}(K_{//})$ is the Bragg peak shape. As a result, $G(\mathbf{k})$ can be rewritten as

$$G(\vec{k}, \vec{K}_{//}) = G_0(K_{\perp})G_{ideal}(K_{//}) + G_{diff}(\vec{k}_{\perp}, \vec{K}_{//}). \qquad \text{(A2-2)}$$

It is easy to get the relationships as follows

$$\iint_{B.Z} G_{ideal}(\vec{K}_{//})d^2K_{//} = \sum_{l} \iint_{B.Z} e^{i\vec{K}_{//}\cdot\vec{r}_l} d^2K_{//} = A_{BZ}, \qquad \text{(A2-3)}$$

$$\iint_{B.Z} G(\vec{k}_{\perp}, \vec{K}_{//})d^2K_{//} = \sum_{l} \left\langle e^{id k_{\perp}(h(\vec{m}+\vec{l})-h(\vec{m}))} \right\rangle \iint_{B.Z} e^{i\vec{K}_{//}\cdot\vec{r}_l} d^2K_{//} = A_{BZ}, \qquad \text{(A2-4)}$$

where $A_{BZ}=a_1^* a_2^*$ is the area of the surface B.Z. By means of Eq.(A2-2), we carry out the integration and obtain the result as follows

$$\frac{1}{A_{BZ}} \iint_{B.Z} G_{diff}(\vec{K}_{//})d^2K = (1 - G_0(\vec{k}_{\perp})). \qquad \text{(A2-5)}$$

In terms of Eq.(2-18), the diffuse intensity, S_{diff}, can be expressed by

$$S_{diff}(k_{\perp}, \vec{K}_{//}) = NF(p)G_{diff}(k_{\perp}, \vec{K}_{//}). \qquad \text{(A2-6)}$$

Because the form factor F(p) varies very slowly in comparison with the structure factor $G(\mathbf{k})$, F(p) may be considered to be approximately constant. Based on Eq.(A2-6), we can obtain

$$\frac{1}{A_{BZ}} \iint_{B.Z} S_{diff}(k_{\perp}, \vec{K}_{//})d^2K_{//} = NF(p)(1 - G_0(k_{\perp})) \qquad \text{(A2-7)}$$

If Eq.(A2-6) is divided by (A2-8), we can further obtain

$$G_{diff}(k_\perp, \vec{K}_{//}) = (1 - G_0(\vec{k}_\perp)) \frac{A_{BZ} S_{diff}(k_\perp, \vec{K}_{//})}{\iint_{B.Z} S_{diff}(k_\perp, \vec{K}_{//}) d^2 K_{//}}. \quad \text{(A2-8)}$$

Inserting Eq.(A2-8) into Eq.(A2-2), we can obtain as follow

$$G(k_\perp, \vec{K}_{//}) = G_0(k_\perp) G_{ideal}(\vec{K}_{//}) + (1 - G_0(\vec{k}_\perp)) \frac{A_{BZ} S_{diff}(k_\perp, \vec{K}_{//})}{\iint_{B.Z} S_{diff}(k_\perp, \vec{K}_{//}) d^2 K_{//}}. \quad \text{(A2-9)}$$

Here, we have proved Eq.(2-21).

Appendix 3:

According to definition, the relative weight, $G_0(k\perp)$, of the Bragg peak may be expressed by

$$G_0(k_\perp) = \sum_{\vec{n}} e^{idk_\perp h(\vec{n})} \sum_{m} e^{-idk_\perp h(\vec{m})} / N^2. \quad \text{(A3-1)}$$

In addition, let us use the probability distribution of the terrace heights to simplify Eq.(A3-1). The sum of scattering phase factors may be expressed by

$$\sum_{\vec{m}} e^{idk_\perp h(\vec{m})} = N \sum_{h} P_h e^{i\phi h}, \quad \text{(A3-2)}$$

where P_h indicates the fraction of atoms at level h and $\phi(=k\perp d)$ is the phase of scattered electron waves. Therefore, $G_0(k\perp)$ may be further written as

$$G_0(k_\perp) = \sum_{h} P_h e^{i\phi h} \sum_{h'} P_h e^{i\phi h'}. \quad \text{(A3-3)}$$

The Eq.(A3-3) may be rewritten as

$$G_0(k_\perp) = \sum_{ll'} P_l P_{l'} \cos(\phi(l - l')). \qquad \text{(A3-4)}$$

Let us assume l-l'=h, and Eq.(A3-4) may be expressed by

$$G_0(k_\perp) = \sum_h (\sum_l P_l P_{l+h}) \cos\phi h. \qquad \text{(A3-5)}$$

As a result, $G_0(k_\perp)$ may be simply denoted as

$$G_0(\vec{k}_\perp) = \sum_h C_h \cos(dk_\perp h), \qquad \text{(A3-6)}$$

where $C_h=\sum P_l P_{l+h}$. Here, we have proved Eq.(2-22).

Appendix 4:

By means of Eq.(2-18), the delta intensity $S_\delta(k_\perp,\mathbf{K}_{//})$ may be expressed as

$$S_\delta(k_\perp, \vec{K}_{//}) = NF(p)G_\delta(k_\perp, \vec{K}_{//}). \qquad \text{(A4-1)}$$

According to Eq.(A2-2), Eq.(A4-1) may be rewritten as

$$S_\delta(k_\perp, \vec{K}_{//}) = NF(p)G_0(k_\perp)G_{ideal}(\vec{K}_{//}). \qquad \text{(A4-2)}$$

Because the form factor F(p) changes very slowly compared with the structure factor, the F(p) factor may be considered to be approximately constant. Eq.(A4-2) is integrated as

$$\iint_{B.Z} S_\delta(k_\perp, \vec{K}_{//}) d^2K = NF(p)G_0(k_\perp) \iint_{B.Z} G_{ideal}(\vec{K}_{//}) d^2K. \qquad \text{(A4-3)}$$

Also, in terms of Eq.(2-18) we can obtain total diffraction intensity as

$$\iint_{B.Z} S(k_\perp, \vec{K}_{//}) d^2K_{//} = NF(p) \iint_{B.Z} G(k_\perp, \vec{K}_{//}) d^2K_{//}. \qquad \text{(A4-4)}$$

Eq.(A4-3) is divided by Eq.(A4-4) and then Eq.(A2-3) and Eq.(A2-4) are inserted. We can derive the result as follows

$$\frac{\iint_{B.Z} S_\delta(k_\perp, \vec{K}_{//}) d^2K_{//}}{\iint_{B.Z} S(k_\perp, \vec{K}_{//}) d^2K_{//}} = G_0(k_\perp). \qquad \text{(A4-5)}$$

Here, we have proved Eq.(2-23).

Appendix 5[40]:

The instrumental resolution is limited by detector aperture size, electron energy spread, and electron beam divergent and so on. Here, we mainly analyse the effect of the detector aperture size.

The detector aperture diameter, d, is 0.1 mm and the distance, l, between the sample and the detector aperture is about 280 mm so we can deduce $\tan(\theta) \approx \theta$. From the geometrical shape, we can obtain

$$\Delta\theta = \frac{d}{l} = \frac{0.1}{280} = 3.6 \cdot 10^{-4} rad. \qquad \text{(A5-1)}$$

From our experiment, we measure that the distance d_1 between (0,0) and (1,0) beams is about 3.5 cm on the LEED screen and that the length l_1 from the sample to screen is about 280 mm. The

deflection voltage V_{10} between (0,0) and (1,0) beams is about 20 V at electron energy 128.5eV.

$$\begin{aligned} &\tan\theta_{10} = \frac{35}{280} = 0.125, \\ &so, \theta_{10} = 0.124 rad \\ &\frac{V_{10}}{\theta_{10}} = \frac{20}{0.124} = 161 V / rad. \end{aligned} \qquad \text{(A5-2)}$$

In terms of Eq.(A5-2) we can figure out the deflection voltage caused by detector aperture size

$$\Delta V = \frac{V_{10}}{\theta_{10}} \Delta\theta = 161 \times 3.6 \cdot 10^{-4} = 58 mV. \qquad \text{(A5-3)}$$

Using the result of Eq.(A5-3), we can calculate the resolution in **k** space. This resolution is

$$\Delta k = \frac{\Delta V}{V_{10}} k_{10} = \frac{58 mV}{20 V} \times 1.0 A^{\circ -1} = 0.003 A^{\circ -1}. \qquad \text{(A5-4)}$$

This result of calculation is consistent with that of experimental measurement(see figure 4.2(a)).

References

1) P. Piercy and B. Grossmann, Kinetics of Annealing of the TiO_2 (110) surface, unpublished, (1998)
2) B. Grossmann and P. Piercy, Phys. Rev. Lett. 74, (1995) 4487
3) B. J. Riel, "Multilayer Adsorption of Water on Rutile (110)" M. Sc. thesis (University of Ottawa, 1997.)
4) B. J. Riel, Review of Selected Properties of Low Dimensional Structure, unpublished, (1998)
5) H. N. Yang, G. C. Wang, T. M. Lu, "Diffraction from Rough Surface and Dynamic Growth Fronts" (World Scientific, Singapore, 1993.)
6) W. W. Mullins, J. Appl. Phys. 30, (1959) 77
7) W. W. Mullins, J. Appl. Phys. 28, (1957) 333
8) G. C. Kuczynski, Trans. Am. Inst. Mining Met. Engrs. 1, (1949) 169
9) H. Lamb, Hydrodynamics (Dover Publications, New York 1945)
10) C. Herring, J. Appl. Phys. 21, (1950) 30
11) A. Rettori and J. Villain, J. Phys. France 49, (1988) 257-267
12) I. M. Lifshitz and V. V. Slyozov, J. Phys. Chem. Solids Pergamon Press 1961. Vol. 19, Nos.1/ 2, pp. 35-50.
13) M. Zinke-Allmang, L.C. Feldman, and M. H. Grabow, Surf. Sci. Report 16(1992) 377-463
14) Makio Uwaha, Journal of Physical Society of Japan Vol. 57. No.5 (1988) 1681-1686
15) P. C. Searson and Rong Li, Phys. Rev. Lett. 74, (1995) 1395-1398
16) W. Selke and T. Bieker, Surf. Sci. 281, (1993) 163-177
17) W. Selke and J. Oitmaa, Surf. Sci. Lett. (1988) 347-352
18) Z. Jiang and C. Ebner, Phys. Rev. B 53 (1996) 11146-11151
19) P. S. Maiya and J. M. Blakely, J. Appl. Phys. 38 (1967) 698-704
20) J. D. Erlebacher and M. J. Aziz, Surf. Sci. 374 (1997) 427-442
21) M. Presicci and T. M. Lu, Surf. Sci. 141 (1984) 233-239
22) J. Wollschlager and M. Henzler, Appl. Phys. A 50 (1990) 57-68
23) Hiroshi Onishi and Yasuhiro Iwasawa, Surf. Sci. 313(1994) L783-789
24) S. Fischer and A. W. Munz at al. Surf. Sci. 337 (1995) 17-30
25) G. Ertl and J. Kuppers, "Low Energy Electrons and Surface Chemistry" (VCH Verlagsgesellschaft, Weinheim, 1985.)

26) P. W. Palmberg and T. N. Rhodin, J. Appl. Phys. 39 (1968) 2425
27) P. W. Palmberg, Appl. Phys. Lett. 13, (1968) 183
28) M. Henzler, Surf. Sci. 73 (1978) 240
29) M. Henzler, Surf. Sci. 11/12 (1982) 450.
30) M. Henzler, Surf. Sci. 152/153 (1985) 963
31) C. S. Lent and P.I Cohen, Surf. Sci. 139 (1984) 121-154
32) P. R. Pukite, C. S. Lent and P. I. Cohen, Surf. Sci. 161 (1985) 39-68
33) R. Altsinger and Henzler, Surf. Sci. 200, 235-240 (1988)
34) J. Wollschlager and M. Henzler, Phys. Rev. B 39, 6052 (1989)
35) J.-K.Zuo and J. F. Wendelken, Phys. Rev. Lett. 70, (1993)1662-1665
36) H.-N. Yang, G.-C. Wang, and T.-M. Lu, Phys. Rev. Lett. 74, (1995) 2276-2279
37) S. J. Chey, et.al., Phys. Rev. Lett. 76, (1996) 3995-3998
38) L. J. Clarke, "Surface Crystallography" (John Wiley & Sons, Chichester, 1985.)
39) P. Piercy, Lecture Notes on Low Energy Electron Diffraction, unpublished (1998)
40) P. Piercy, Calculation Notes on Low Energy Electron Diffraction, unpublished, (1995)
41) SPA-LEED System, USER'S MANUAL(LEYBOLD AG, Koln, Germany 1991)